Developments in Mössbauer Spectrometry: From Instrumentation to High Pressure Studies on Spins and Phonons

Thesis by
Pedro Guzman

In Partial Fulfillment of the Requirements for the
Degree of
Doctor of Philosophy

CALIFORNIA INSTITUTE OF TECHNOLOGY
Pasadena, California

2024
Defended March 21, 2024

Pedro Guzman
ORCID: 0000-0002-9726-8315

ACKNOWLEDGEMENTS

I would like to start by thanking my advisor, Brent Fultz. I am very grateful for the guidance, encouragement, support, and mentorship you have provided throughout my doctoral journey at Caltech. Your commitment and dedication to advancing my intellectual growth has been instrumental in shaping both my research and personal development. Your constructive feedback and insightful suggestions has been invaluable in refining my ideas and pushing the boundaries of my research. Your mentorship extended beyond the academic field and I am appreciative for the privilege of having you as my advisor.

The instrumentation work in this thesis was done in collaboration with Valerie Scott and Risaku Toda from Jet Propulsion Laboratories. This work would not have been possible without their tremendous effort and guidance. Additionally, I would like to thank my former Fultz group member Cullen Quine, whose effort and assistance in electronics for this project was particularly valuable.

The high-pressure experimental data in this thesis was collected at the Advanced Photon Source at Argonne National Laboratory. I would like to thank the all beam-line scientist who were instrumental in conducting the high-pressure experiments reported in this thesis. In particular, I want to thank Guoyin Shen of HPCAT and Jiyong Zhao, Barbara Lavina, Michael Hu, and Ercan Alp of Sector 3. Thank you to my former Fultz group members Stefan Lohaus, who joined me on various beamtimes and showed me all about diamond anvil cells, and Camille Bernal, who

assisted on various beamtimes.

Thanks to my thesis committee, Brent Fultz, Kathy Faber, Valerie Scott, and Joseph Falson for taking the time to guide me during my defense process. Also, I would like to thank my undergraduate advisor, Stuart Brown, who introduced me to experimental research in condensed matter physics and encouraged me to pursue a graduate degree.

To my other former and current Fultz group members, Joel Chacko, Vladimir Ladygin, Elizabeth Zhou, Ziyi Wang, Claire Saunders, Elena Priesen Reis, Kyle Hunady, David Boyd, and Channing Ahn, I want to thank you for all the insightful discussions an making my time at Caltech gratifying. Also, I would like to thank the administrative assistants, Catherine Pichotta, Christy Jenstad, and Jennifer Blankenship, for all their help and countless conversations.

To my parents, Angelita and Pedro, your love, support, and encouragement has been central to my success. Your hard work and dedication has always inspired me and I carry with me the values and lessons you have instilled in me. I am forever grateful for the sacrifices you have made to shape my future and I am fortunate to have you both as my parents. To my siblings, Martha, Rosa, Fernando, and Angelica, your selfless acts of support and willingness to lend a helping hand in times of need did not go unnoticed. I am thankful to have siblings like you all who celebrate my achievements and have been a source of joy and love.

Finally, I would like to thank my wife, Meliza Guzman. I want to express my heartfelt gratitude for being my source of inspiration throughout this journey. Your

encouragement and understanding have played a pivotal role in helping me overcome obstacles and reach this point. Thank you for your patience during the long hours of work and for standing by me during the moments of self-doubt. Your belief in me has been my driving force, pushing me to persevere and excel in my academic pursuits. Your love, sacrifices, and endless support have made this journey not only bearable but truly meaningful. You are my everything.

Financial support for the work in this thesis was provided by the California Institute of Technology, the National Science Foundation (NSF) grant no. 1904714, and NSF Graduate Research Fellowship DGE-1745301.

ABSTRACT

The well-established technique of ^{57}Fe Mössbauer spectrometry is used to investigate the local chemical environment in iron-containing materials. This technique relies on the recoil-free emission and absorption of γ-rays by resonant nuclei within a solid. The key component of a Mössbauer spectrometer is the velocity Doppler drive, which modulates the energy of the incident γ-rays to detect the hyperfine structure of resonant nuclei. Since the 1970s, the conventional velocity Doppler drive has been constructed using a pair of electromagnetic coils, one for power and the second for feedback. An alternative Mössbauer spectrometer was developed, utilizing an amplified piezoelectric actuator as the Doppler velocity drive under feedback control. The actuator, driven with a quadratic displacement waveform, produced a linear velocity profile and was optimized using measurements from a laser Doppler vibrometer (LDV). In transmission geometry, ^{57}Fe Mössbauer spectra of α-iron display minimal peak distortions, enabling Mössbauer spectrometry in applications requiring compact size and low mass, such as geochemical studies on the Moon, Mars, or asteroids.

Synchrotron radiation is used for numerous experimental techniques, including X-ray diffraction (XRD), nuclear resonant inelastic X-ray scattering (NRIXS), and nuclear forward scattering (NFS), also known as synchrotron Mössbauer spectrometry. Diamond-anvil cells, capable of reaching high pressures at various temperatures, combined with synchrotron experimental methods, provide the means to investigate

the vibrational, magnetic, and thermophysical properties of materials. Measurements on $^{57}Fe_{55}Ni_{55}$ were conducted using synchrotron XRD, NRIXS, and NFS under various pressures and temperatures. XRD measurements at 298 K and 392 K under pressures up to 20 GPa confirmed a pressure-induced Invar effect between 7 GPa and 13 GPa, where the coefficient of thermal expansion is nearly zero. NFS measurements revealed a decrease in the magnetic moment of ^{57}Fe under pressure, indicating an increase in magnetic entropy. The ^{57}Fe phonon density of states (DOS) was measured with NRIXS and gave a phonon entropy. Using thermodynamic Maxwell relations, magnetic and phonon contributions to thermal expansion were determined, demonstrating that the low thermal expansion in the pressure-induced Invar region stems from a competition between the thermal expansion from spins and from phonons.

PUBLISHED CONTENT AND CONTRIBUTIONS

[1] **P. Guzman**, C. Quine, S. Lohaus, L. Schul, R. Toda, V. Scott, and B. Fultz, "A miniaturized piezoelectric mössbauer spectrometer with feedback control," *Review of Scientific Instruments*, vol. 94, no. 11, 2023,
P.G. assembled mechanical hardware, planned and performed experiments, analyzed the data, and wrote the manuscript. [Online]. Available: https://doi.org/10.1063/5.0157651

[2] **P. Guzman**, S. Lohaus, C. Bernal-Choban, J. Zhao, G. Shen, B. Lavina, M. Hu, E. Alp, and B. Fultz, "The Pressure Induced Invar Effect in $Fe_{55}Ni_{45}$: An Experimental Study with Nuclear Resonant Scattering," *Submitted to Physical Review B*,
P.G. planned and performed experiments, analyzed the data, and wrote the manuscript.

[3] S. H. Lohaus, M. Heine, **P. Guzman**, C. M. Bernal-Choban, C. N. Saunders, G. Shen, O. Hellman, D. Broido, and B. Fultz, "A thermodynamic explanation of the invar effect," *Nature Physics*, vol. 19, no. 11, pp. 1642–1648, 2023,
P.G. assisted with experiments and contributed to the manuscript. [Online]. Available: https://doi.org/10.1038/s41567-023-02142-z

TABLE OF CONTENTS

Chapter 1

INTRODUCTION

1.1 The Mössbauer Effect

The technique known as Mössbauer spectrometry can be used to investigate the local chemical environment of resonant nuclei, including structural, electronic, and magnetic properties. Materials are probed by Mössbauer spectrometry from the perspective of the resonant nuclei looking out. Recoilless nuclear resonant scattering, initially identified in solid ^{191}Ir, was first observed during the doctoral research carried out by Rudolf Mössbauer in 1958. The Nobel Prize in physics was presented to him in 1961 for the discovery [1].

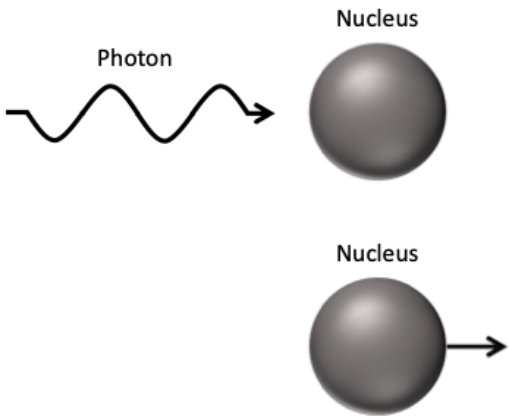

Figure 1.1: (Upper) Incident photon approaching free nucleus. (Lower) Recoil of free nucleus after being hit by a photon.

Recoil-Free Fraction

The Mössbauer effect is the recoil-free emission and absorption of γ-rays by atomic nuclei that are bound in a solid [2, 3]. The recoilless fraction, considered a crucial element of the Mössbauer effect, is founded on the likelihood that, during the emission or absorption of γ-rays, a nucleus undergoing a nuclear transition will not experience recoil. The occurrence of recoil results from the conservation of momentum, wherein a nucleus emitting or absorbing a γ-ray undergoes recoil in the opposite direction to conserve momentum. The kinetic energy of the emitted γ-ray diminishes the energy of the recoil, denoted as E_{R}.

$$E_R = \frac{E_\gamma^2}{2Mc^2} \approx 2meV \tag{1.1}$$

The γ-ray energy is represented by E_γ, the nuclear mass by M, and the speed of light by c. In a free nucleus of ^{57}Fe, E_γ is 14.41 keV, and M is 94.62x10^{-27} kg, resulting in a recoil energy E_{R}, free of approximately 2 meV. This value is six orders of magnitude larger than the line width of the nuclear resonance of ^{57}Fe, which is around 10^{-9} eV, preventing the occurrence of nuclear resonant absorption. The recoil of a free nucleus due to the collision with a photon is depicted in Fig. 1.1.

For a nucleus bound in a solid, the recoil is absorbed by the entire solid, not just by the ^{57}Fe nuclei. The recoil energy is now expressed as $E_{\mathrm{R,free}}/N$, where N is the number of atoms in the solid, and for 1 mole of atoms, N is approximately 10^{23}. In a solid, the recoil energy is considered negligible, enabling the possibility of nuclear resonant absorption.

The Einstein model of lattice vibrations is characterized by a single phonon fre-

quency, denoted as ω_E. Therefore, the Mössbauer effect can be observed under the condition

$$E_{R,free} \ll \hbar\omega_E = k_B\theta_E \tag{1.2}$$

where k_B is the Boltzman constant, and θ_E is the Einstein temperature. Under the Einstein model, the Mössbauer-Lamb factor, which describes the probability of recoilless nuclear absorption or emission to happen, is approximately

$$f_{ML} \approx 1 - \frac{E_{R,free}}{\hbar\omega_E} \approx exp\left(\frac{E_{R,free}}{k_B\theta_E}\right). \tag{1.3}$$

The Debye model yields a more accurate Mössbauer-Lamb factor [4]

$$f_{ML} = exp\left[-\frac{3E_{R,free}}{2k_B\theta_D}\left(1 + \frac{4T^2}{\theta_D^2}\int_0^{\theta_D/T}\frac{x}{e^x - 1}\,dx\right)\right]. \tag{1.4}$$

where θ_D is the Debye temperature. The Mössbauer effect is most easily observed when f_{ML} is large. The exponential decrease of the Mössbauer-Lamb factor with $E_{R,free}$ and γ-ray energy means that recoilless nuclear absorption or emission is more probable for isotopes with excited states at low energies, including ^{57}Fe. This makes ^{57}Fe Mössbauer spectroscopy particularly useful for studying iron-containing materials [5]. The Mössbauer effect is not limited to the ^{57}Fe isotope and has also been observed in isotopes such as ^{119}Sn, ^{121}Sb, ^{151}Eu, and ^{191}Ir.

Hyperfine Interactions

The recoil-free emission or absorption of γ-rays in ^{57}Fe occurs between the ground state of spin $I = 1/2$ and the excited state of spin $I = 3/2$, with an energy of 14.4 keV. Nevertheless, the surrounding electrons can influence the nuclear energy levels of the resonant nuclei. Perturbations to the nuclear energy levels can be detected

by the Mössbauer effect, making Mössbauer spectrometry an ideal technique for investigating the local electronic environment of the resonant atom. The 14.4 keV excited state of ^{57}Fe possesses a half-life of 98 ns, resulting in an absorption linewidth of 4.67x10^{-9} eV due to the uncertainty principle.

$$\Delta E = h/\Delta t \tag{1.5}$$

where h is the Planck constant and t is the lifetime of the excited nuclear state.

In addition to the recoil-free fraction, the most useful measurable quantities in Mössbauer spectrometry for characterizing materials with Mössbauer active nuclei are the hyperfine interactions. The description of the valuable information that can be extracted from the three hyperfine parameters (the isomer shift, the electric quadrupole splitting, and the hyperfine magnetic field) is now provided.

Isomer Shift The isomer shift (IS) is determined by the electron density at the resonant nuclei, resulting from a Coulomb interaction between the nuclear and electronic charge distributions [2, 3, 5]. This shift requires electrons to have a finite probability of being within the nucleus, restricting interactions to s-electrons. The energy level is shifted by the Coulomb interaction between the s-electron density and the nuclear charge

$$\delta E = \frac{2}{3}\pi Z e^2 |\Psi_S(0)|^2 \langle R \rangle^2 \tag{1.6}$$

where Z is the atomic number, Ψ_s is the s-electron density, and $\langle R \rangle$ is the mean-square radius of the nuclear charge distribution. The overall shift observed in Mössbauer spectrometry is created by differences in the s-electron density between

the source (S) and absorber (A)

$$\delta E = \frac{2}{3}\pi Z e^2 \left(|\Psi_A(0)|^2 - |\Psi_S(0)|^2\right) \left(\langle R\rangle_E^2 - \langle R\rangle_G^2\right) \tag{1.7}$$

where subscripts G and E refer to the ground and excited states. Useful information about the local chemical environment near the resonant nuclei of the absorber is provided by the isomer shift, and it is commonly used for the identification of oxidation states and spin.

Electric Quadrupole Splitting The electric quadrupole splitting (QS) arises from the interaction between the electric field gradient (EFG) and the non-spherical shape of a nucleus, characterized by its nuclear quadrupole moment (Q) [2, 3, 5]. Spherical symmetry and $Q = 0$ are observed in nuclei with spin quantum numbers $I = 0$ or $I = 1/2$. For a nucleus with a spin quantum number $I > 1/2$, a deviation from spherical symmetry occurs, leading to a non-zero Q. In such cases, when Q is exposed to an asymmetric EFG, the nuclear energy levels experience a loss of degeneracy due to the electric quadrupole interaction. The Hamiltonian eigenvalues for the interaction between Q and the EFG are

$$E_Q = \frac{eQV_{zz}}{4I(2I-1)}\pi Z e^2 \left[3m_I^2 - I(I+1)\right] \left(1 + \frac{\eta^2}{3}\right)^{1/2} \tag{1.8}$$

$$m_I = I, I-1, ..., -|I| \tag{1.9}$$

where V_{zz} is the principal eigenvalue of the EFG tensor, I is the nuclear angular momentum, and η is the asymmetry parameter,

$$\eta = \frac{V_{xx} - V_{yy}}{V_{zz}}. \tag{1.10}$$

The energy for resonant absorption is split into two lines, as only the excited state has distinct eigenvalues for the Hamiltonian, with the difference

$$\Delta E_Q = \frac{1}{2} eQV_{zz}\sqrt{1+\frac{\eta^2}{3}}. \tag{1.11}$$

Changes in local symmetry and valence differences near the resonant nuclei will lead to shifts in QS in various Fe-containing materials. Figure 1.2 shows a nuclear energy diagram for quadrupole splitting in ^{57}Fe.

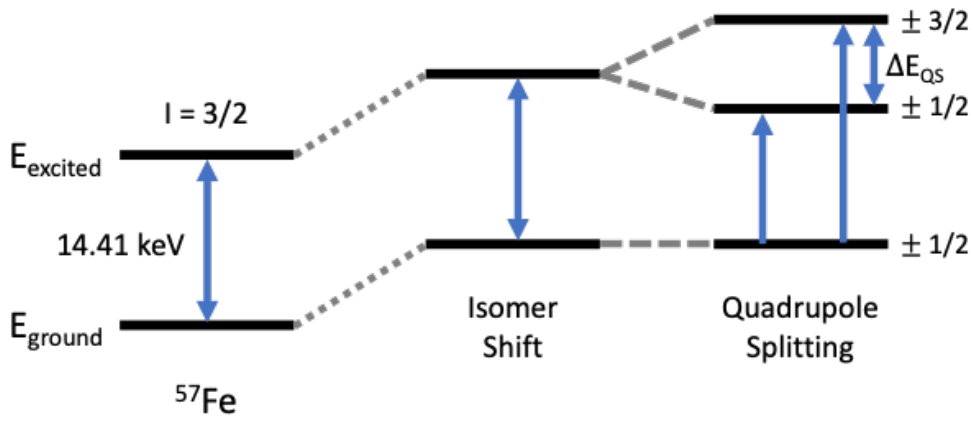

Figure 1.2: Nuclear energy diagram of the isomer shift and quadrupole splitting for ^{57}Fe.

Hyperfine Magnetic Field The hyperfine magnetic field (HMF) occurs when the magnetic moment of the nucleus, μ, interacts with the effective magnetic field (B_{eff}) produced by nearby electrons [3, 5]. As a result of this interaction, the nuclear energy levels undergo splitting into $(2I + 1)$ components, owing to the nuclear Zeeman effect. The Hamiltonian governing the interaction between μ and B_{eff} is

$$H_{HMF} = -\overrightarrow{\mu} \cdot \overrightarrow{B_{eff}} = -g\mu_N \overrightarrow{I} \cdot \overrightarrow{B_{eff}} = -g\mu_N B I_z \tag{1.12}$$

where g is the nuclear gyromagnetic ratio, μ_N is the nuclear magneton, and I_z is the z-component of the nuclear spin I, which can take on the values of $-I, -I+1, \ldots, I-1, I$. In the case of ^{57}Fe, the ground state, with a spin of $I = 1/2$, undergoes a split into two sublevels, while the excited state, with a spin of $I = 3/2$, undergoes a split into four sublevels. However, only six transitions are permitted overall, as dictated by the selection rules: $\Delta I = 1$; $\Delta m = 0, \pm 1$. The splitting of the nuclear energy levels is influenced by the hyperfine magnetic fields, which are determined by the local chemical environment surrounding the resonant nuclei. The transitions between the ground state and the excited state of ^{57}Fe in a hyperfine magnetic field are shown in Figure 1.3.

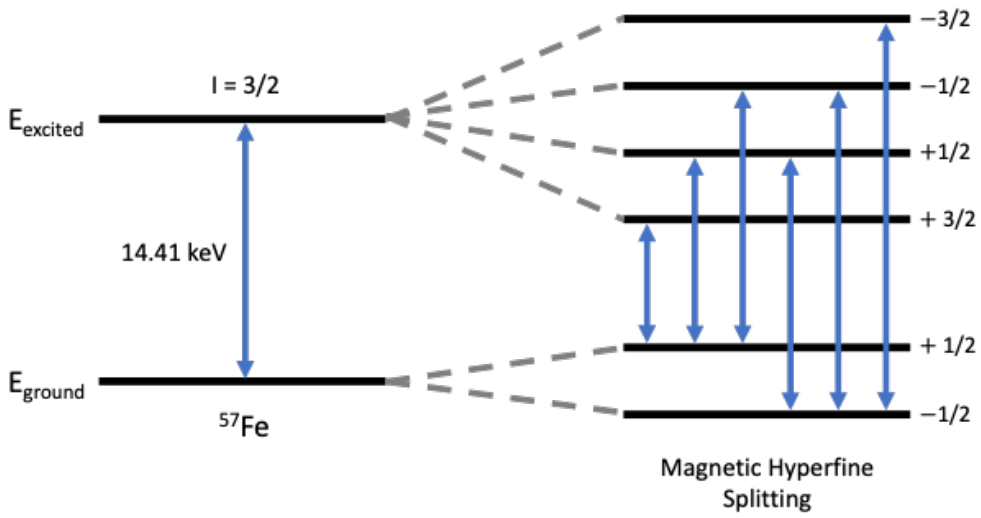

Figure 1.3: Nuclear energy splitting and transitions between the ground state and the first excited state of an ^{57}Fe nucleus in a hyperfine magnetic field.

Mössbauer Spectrum of α-Fe

At room temperature, pure iron is magnetic, has a bcc crystal structure, and a hyperfine magnetic field (HMF) of 33 T. A sextet is observed in the Mössbauer spectrum of pure bcc Fe, shown in Fig. 1.4, owing to the negligible electric quadrupole splitting resulting from symmetry. The spectrum in Fig. 1.4 is symmetric, with its center located at velocity, $v = 0$ (albeit with an isomer shift present). This is due to the utilization of bcc Fe as a calibration, causing all shifts detected in other Fe-containing samples to be referenced to bcc Fe.

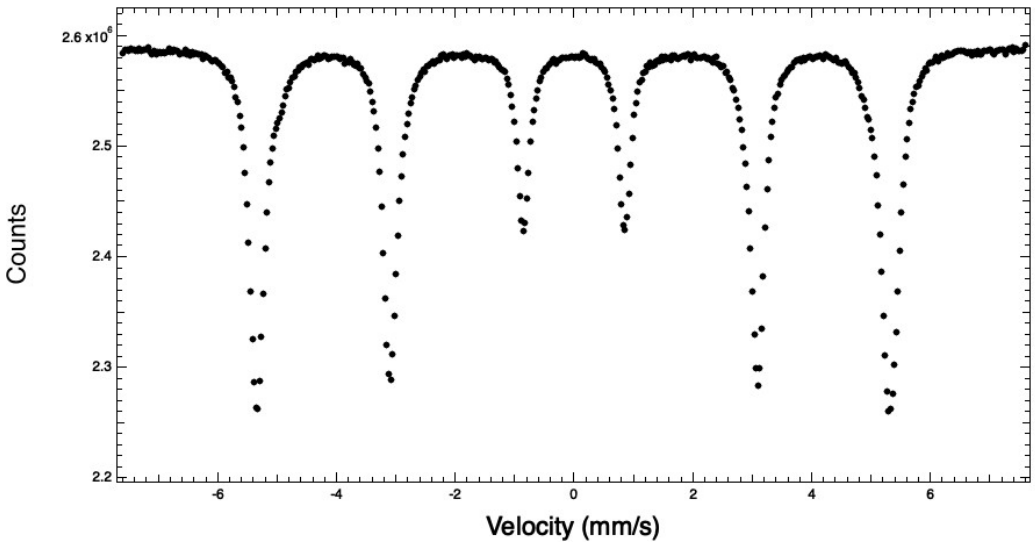

Figure 1.4: Mössbauer spectrum of a 30μm thick α-Fe foil measured in transmission geometry.

The width of the observed peaks in bcc Fe is influenced by both the linewidth of the excited nuclear state and instrumental broadening. However, the orientation of the HMF with respect to the propagation direction of the γ-rays defines the relative

intensities [3]. A isotropic distribution of HMF will produce relative intensities

$$I_1 : I_2 : I_3 : I_4 : I_5 : I_6 = 3 : 2 : 1 : 1 : 2 : 3. \tag{1.13}$$

When the orientation of the HMF is parallel to the propagation direction of the γ-rays the relative intensities are

$$I_1 : I_2 : I_3 : I_4 : I_5 : I_6 = 3 : 0 : 1 : 1 : 0 : 3. \tag{1.14}$$

When the orientation of the HMF is perpendicular to the to the propagation direction of the γ-rays the relative intensities are

$$I_1 : I_2 : I_3 : I_4 : I_5 : I_6 = 3 : 4 : 1 : 1 : 4 : 3. \tag{1.15}$$

The presence of magnetic texture is commonly observed in foil samples of bcc Fe, and variation can be seen among samples. Nevertheless, the robustness of the hyperfine splitting observed in the sextet of bcc Fe is consistent.

Mössbauer Spectrometry on Mars

The MIMOS II miniature Mössbauer spectrometer played a crucial role in advancing our understanding of Martian geology through Mössbauer studies on the Mars Exploration Rovers, Spirit and Opportunity, which launched in 2003. Developed in collaboration with institutions like NASA by Dr. Göstar Klingelhöfer and his group at the University of Mainz, this pioneering instrument utilized Mössbauer spectroscopy, providing important insights into the mineral composition of rocks and soils. MIMOS II, equipped on both Spirit and Opportunity, allowed the Martian surface to be analyzed by characterizing iron-bearing minerals and providing valuable data for scientists to comprehend past environmental conditions on Mars. Most

notably, a substantial amount of goethite (α-FeOOH), formed only in an aqueous environment, was revealed in the MIMOS II Mössbauer spectra collected on the Red Planet, suggesting a past presence of water on Mars [6–9].

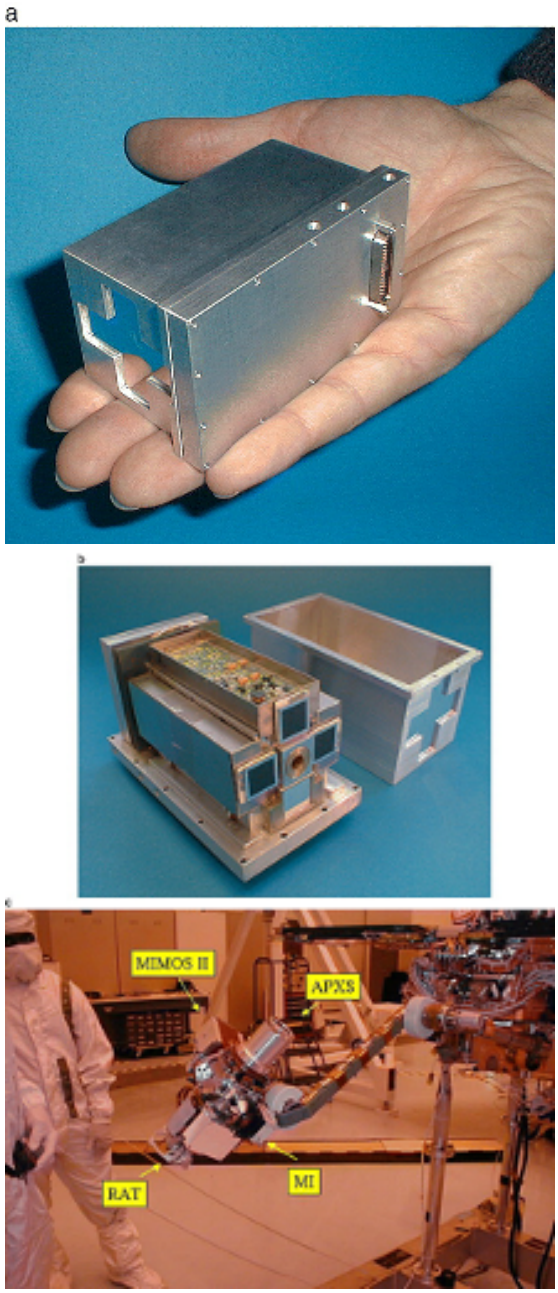

Figure 1.5: (Upper) Overall view of the MIMOS II sensor head. (Middle) MIMOS II sensor head with cover taken off displaying interior and front view of the collimator surrounded by four Si-PIN detectors. (Lower) View of the MIMOS II sensor head mounted on the turret. [6]

The MIMOS II, a miniature electromagnetic velocity Doppler drive, was equipped with two ^{57}Co Mössbauer sources and had an approximate mass of 500 grams. The reference source, utilizing hematite (alpha-Fe2O3) and iron (alpha-Fe) as targets, was mounted at one end of the MIMOS II in transmission geometry with a PIN-diode detector for calibration purposes. At the opposite end of the MIMOS II, a source was utilized to irradiate the surface on Mars and analyze the soil and rocks. The analysis end of the MIMOS II operated in backscatter geometry, combining four PIN-diode detectors to collect the backscattered ^{57}Fe photons [6]. Multiple views of the MIMOS II, developed by Dr. Göstar Klingelhöfer, are depicted in Figure 1.5.

1.2 Synchrotron Radiation

The largest synchrotron in the United States is measured at a circumference of 1.1 km and is known as the Advanced Photon Source (APS), located at Argonne National Lab (ANL) in Argonne, Illinois (refer to Fig. 1.6). Within the APS, synchrotron radiation is generated by a large evacuated storage ring where electrons are circulated. Prior to injection into the storage ring, the electrons undergo acceleration first through a linear accelerator and then through a booster synchrotron, using electromagnets to achieve speeds near the speed of light and reaching energies of approximately 7 GeV. The emission of synchrotron radiation occurs continuously as the electrons are in orbit.

The storage ring includes 40 straight sections, with the beam being redirected between these sections by bending magnets. These straight sections incorporate linear arrays of magnets with alternating polarity, known as undulators, causing

rapid oscillations of electrons along sinusoidal paths, as shown in Fig. 1.7. The spacing between these magnets defines the energy of the radiation, allowing for precise tuning tailored to the requirements of the experiment. [10, 11]

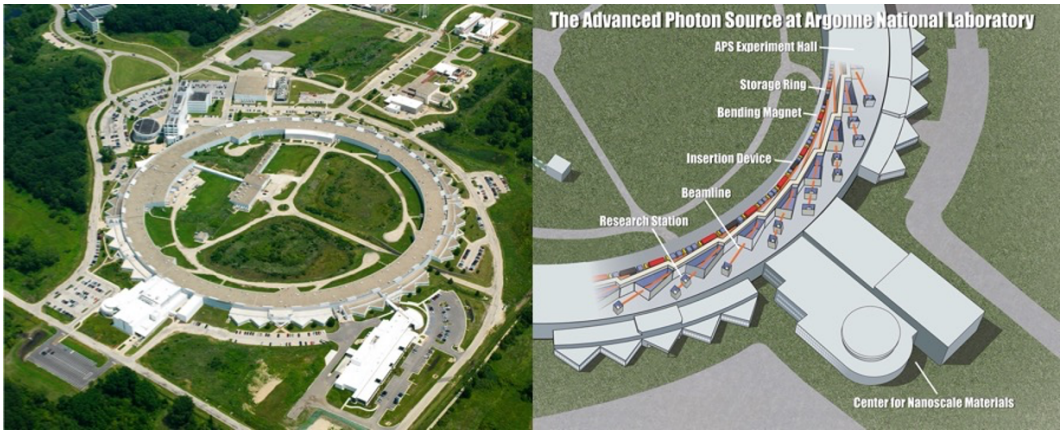

Figure 1.6: (Left) Aerial view of the Advance Photon Source (APS) synchrotron storage ring at Argonne National Laboratory (ANL). (Right) Schematic of the beamline setup at the APS where experiments take place in the straight sections. Images extracted from [12].

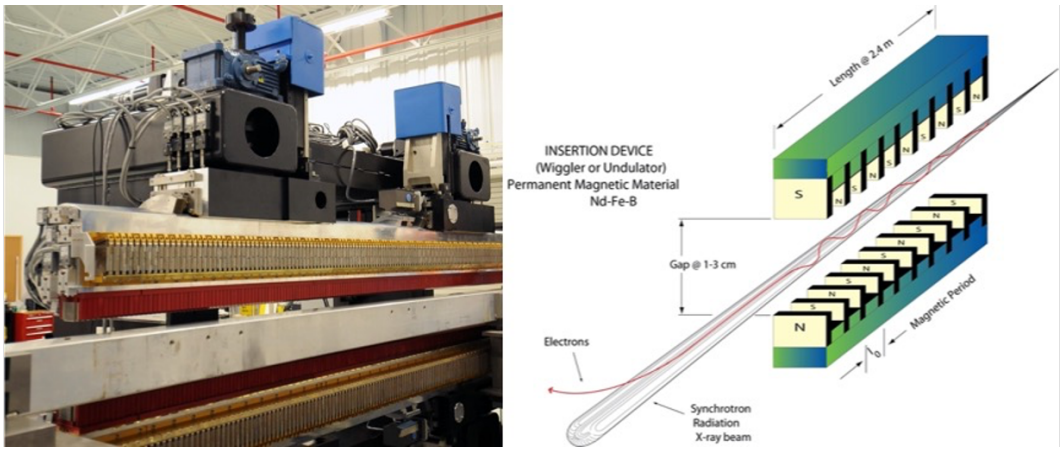

Figure 1.7: (Left) Image of undulator insertion device at the Advanced Photon Source (APS) at Argonne National Laboratory (ANL). (Right) Schematic representation of the working principle behind the undulator insertion device. Images adapted from [12].

Synchrotron X-Ray Diffraction

Crystal structures, lattice parameters, and crystal defects can be determined using the robust technique known as X-ray diffraction (XRD). In order for diffraction to happen, the wavelengths of the incident waves must be on the same order as interatomic spacings in the crystal. In high-pressure XRD experiments, samples

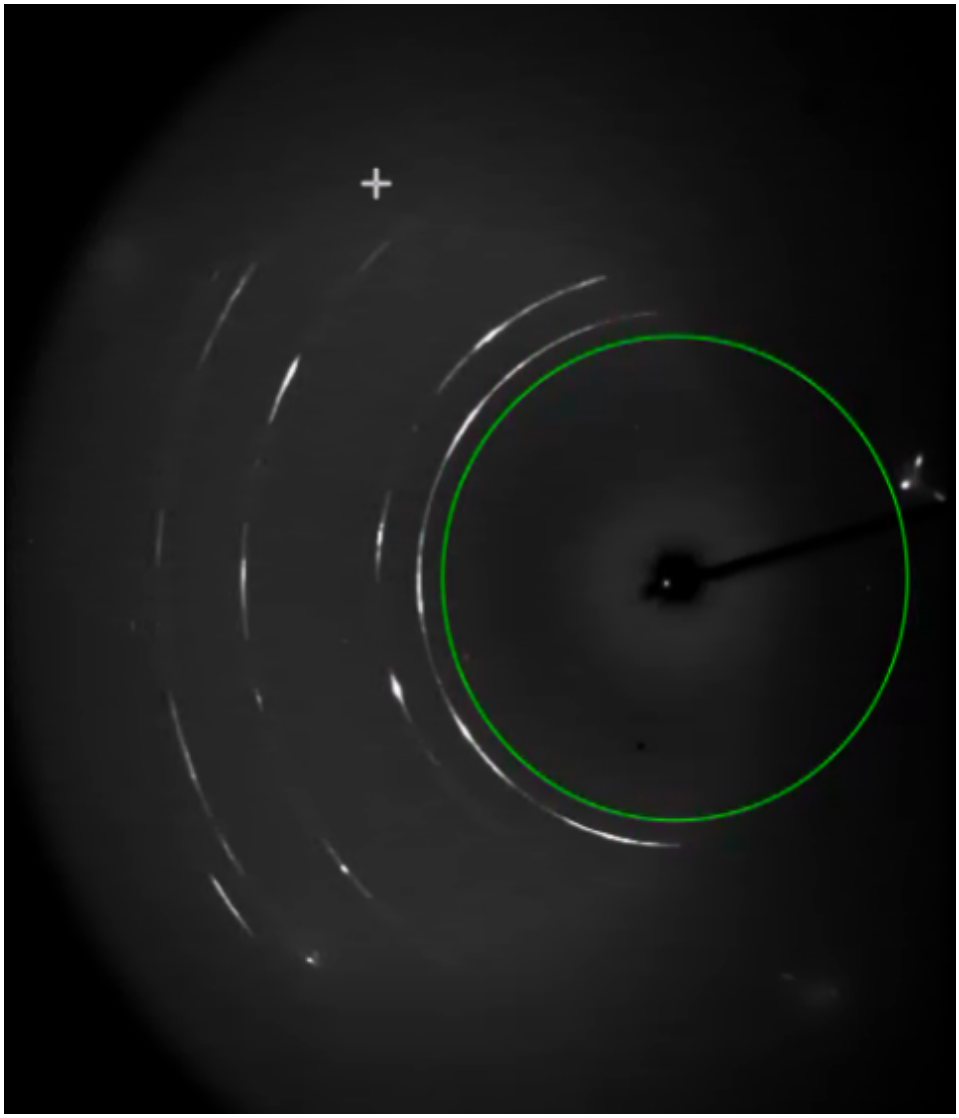

Figure 1.8: Ring diffraction pattern collected with CCD detector.

that are tens of microns in size are required, making synchrotron radiation the

ideal method for such experiments. A complete diffraction pattern is obtained within seconds through the utilization of a two-dimensional charged-coupled device (CCD) area detector. In the case of polycrystalline samples, the raw data is shown as a collection of ring diffraction patterns (refer to Fig. 1.8). The radii of the measured rings are proportional to the different interplanar spacings, d_{hkl}, of diffracting planes labeled by Miller indices (hkl) in accordance with Bragg's law,

$$\lambda = 2d_{hkl}sin(\theta_{hkl}). \tag{1.16}$$

The raw data image file is converted to a conventional one-dimensional diffraction pattern suitable for analysis of crystal structure and unit cell volume. The processing of the two-dimensional X-ray diffraction CCD data is carried out using the Dioptas software package [13].

Synchrotron Mössbauer Spectrometry

Synchrotron Mössbauer spectrometry or nuclear forward scattering (NFS) is recognized as the time domain equivalent to traditional Mössbauer spectrometry, where the absorption lines of resonant nuclei are measured as a function of energy. The incident photon beam is filtered and tuned to the resonant energy, 14.4 keV for ^{57}Fe, using a monochromator, followed by the utilization of a high-resolution monochromator to achieve a meV bandwidth. The excitation of all resonant nuclei occurs simultaneously through a synchrotron flash. At the advanced photon source (APS), the synchrotron radiation is produced in the form of a series of 24 pulses with a duration of 70 ps, separated by 153.3 ns intervals. With the electronic scattering lifetime on the order of femtoseconds, this temporal arrangement allows for the iso-

lation and detection of the scattering attributed to the nuclear resonant state, which has a lifetime of 141 ns. [14]

As the resonant nuclei decay to their ground state, recoil-free photons with marginally different frequencies are emitted. The interference of these emitted photons results in the generation of beats due to the superposition of their frequencies. The time-resolved interference pattern, referred to as quantum beats, enables the extraction of information on hyperfine interactions. Figure 1.9 displays an NFS spectrum of $^{57}Fe_{55}Ni_{45}$ measured at the APS.

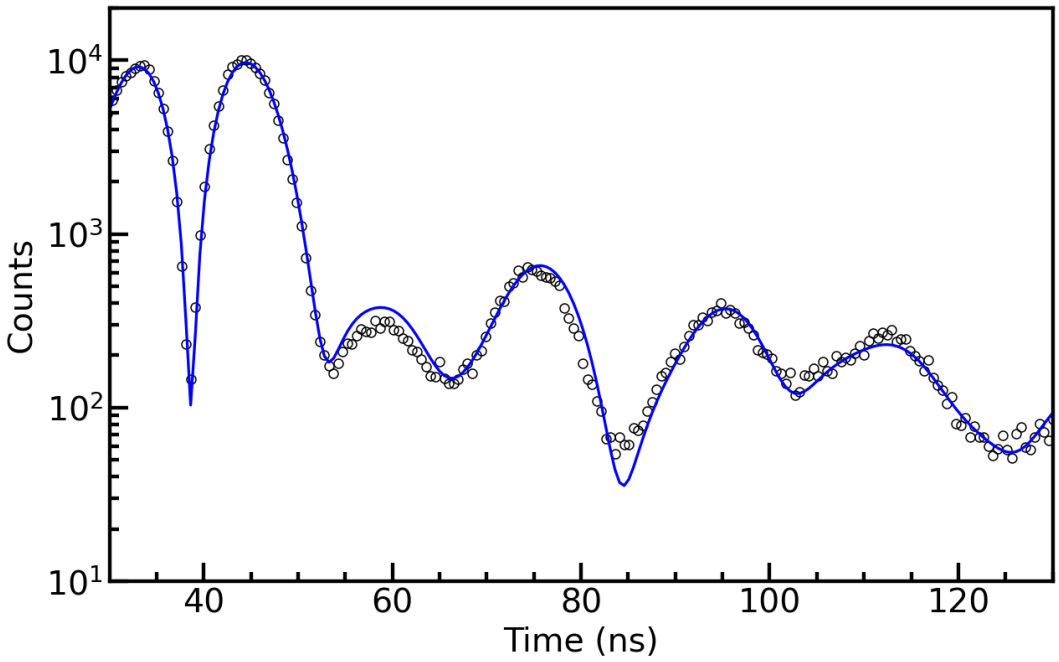

Figure 1.9: NFS spectrum from $^{57}Fe_{55}Ni_{45}$ at room temperature and a pressure of 0.5 GPa. The fit to the data with the software CONUSS is in blue.

Quantum beats occur when the presence of splitting in nuclear energy levels is observed within resonant nuclei, leading to the emission of photons with varying frequencies. In resonant nuclei containing a HMF, such as ^{57}Fe, six allowable

transitions arise from the energy splitting, resulting in the creation of complex interference beats. The considerable separation in energy attributed to the HMF gives rise to the observation of beats with short time periods in magnetic samples [14, 15]. As temperature or pressure increases, causing the loss of long-range magnetic order, the period of quantum beats increase and eventually are nonexistent. The analysis of NFS spectra requires the utilization of the specialized software program CONUSS [16].

Nuclear Resonant Inelastic X-Ray Scattering

Nuclear resonant inelastic X-ray scattering (NRIXS) is an exclusive synchrotron technique used to probe the partial phonon densities of states (pDOS) of the resonant nuclei at high pressures. In NRIXS, we perform a scan in energy of the incident

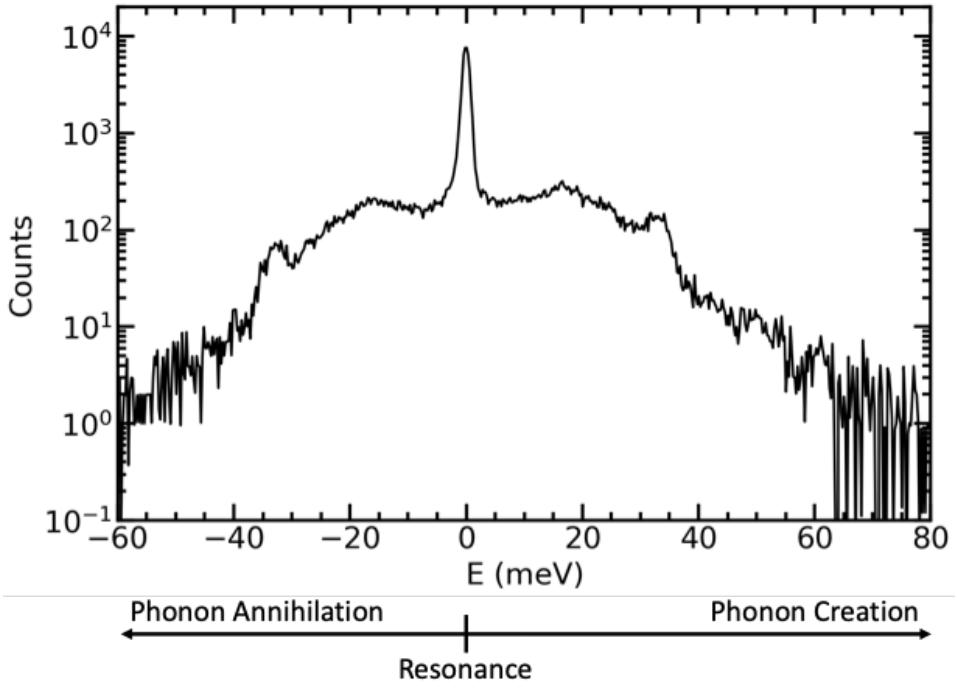

Figure 1.10: NRIXS spectrum from $^{57}Fe_{55}Ni_{45}$ at ambient conditions.

photons varying tens of meV above and below the nuclear resonance energy. Away from resonance, the photons are able to scatter inelastically and either gain or lose the energy required to excite the nuclear transition of the resonant nuclei, therefore annihilating or creating phonons in the material [14, 15]. The detection of resonant events as a function of energy detuned from resonance is the aim of NRIXS experiments. The analysis of NRIXS data, which is the number of inelastic incoherent scattering events at each detuned energy, to a phonon pDOS requires the use of the specialized software program PHOENIX [16]. Figure 1.10 shows the raw NRIXS spectrum for $^{57}Fe_{55}Ni_{45}$ at ambient conditions.

References

[1] R. L. Mössbauer, "Nobel Lecture in Physics," https://www.nobelprize.org/uploads/2018/06/mossbauer-lecture.pdf, 1961.

[2] R. Cohen, *Applications in Mössbauer Spectroscopy*. Elsevier, 1976.

[3] F. J. Berry and D. P. Dickson, *Mössbauer Spectroscopy*. Cambridge University Press Cambridge, 1986.

[4] R. Pound and G. Rebka Jr, "Variation with temperature of the energy of recoil-free gamma rays from solids," *Physical Review Letters*, vol. 4, no. 6, p. 274, 1960.

[5] B. Fultz, "Mössbauer Spectrometry," *in Characterization of Materials, E. Kaufmann, Ed.*, pp. 1–21, Wiley, 2012.

[6] G. Klingelhoefer, R. V. Morris, B. Bernhardt, D. Rodionov, P. A. de Souza, S. W. Squyres, J. Foh, E. Kankeleit, U. Bonnes, R. Gellert *et al.*, "Athena MIMOS II Mössbauer spectrometer investigation," *Journal of Geophysical Research: Planets*, vol. 108, no. E12, p. 8067, 2003.

[7] G. Klingelhoefer, E. DeGrave, R. V. Morris, A. Van Alboom, V. G. de Resende, P. De Souza, D. Rodionov, C. Schröder, D. W. Ming, and A. Yen, "Mössbauer spectroscopy on Mars: goethite in the Columbia Hills at Gusev crater," *Hyperfine Interactions*, vol. 166, pp. 549–554, 2005.

[8] G. Klingelhöfer, D. Rodionov, R. Morris, C. Schröder, P. deSouza, D. Ming, A. Yen, B. Bernhardt, F. Renz, and I. Fleischer, "MIMOS II on MER One

Year of Mossbauer Spectroscopy on the Surface of Mars: From Jarosite at Meridiani Planum to Goethite at Gusev Crater," *Lunar and Planetary Science XXXVI, Part 11*, p. 2349, 2005.

[9] R. V. Morris, G. Klingelhoefer, C. Schröder, D. S. Rodionov, A. Yen, D. W. Ming, P. A. de Souza, I. Fleischer, T. Wdowiak, R. Gellert *et al.*, "Mössbauer mineralogy of rock, soil, and dust at Gusev crater, Mars: Spirit's journey through weakly altered olivine basalt on the plains and pervasively altered basalt in the Columbia Hills," *Journal of Geophysical Research: Planets*, vol. 111, p. E02S13, 2006.

[10] E. Alp, T. Mooney, T. Toellner, and W. Sturhahn, "Nuclear resonant scattering beamline at the advanced photon source," *Hyperfine interactions*, vol. 90, no. 1, pp. 323–334, 1994.

[11] Argonne National Laboratory, "7-GeV Advanced Photon Source Instrumentation Initiative Conceptual Design Report," Tech. Rep., 1992.

[12] Argonne National Laboratory, Advanced Photon Source, *Image Bank*. [Online]. Available: https://www.flickr.com/photos/97432701@N03/albums/72157634111853722/

[13] C. Prescher and V. B. Prakapenka, "DIOPTAS: a program for reduction of two-dimensional X-ray diffraction data and data exploration," *High Pressure Research*, vol. 35, no. 3, pp. 223–230, 2015.

[14] W. Sturhahn, "Nuclear resonant spectroscopy," *Journal of Physics: Condensed Matter*, vol. 16, no. 5, p. S497, 2004.

[15] A. Chumakov and W. Sturhahn, "Experimental aspects of inelastic nuclear resonance scattering," *Hyperfine interactions*, vol. 123, no. 1-4, pp. 781–808, 1999.

[16] W. Sturhahn, "CONUSS and PHOENIX: Evaluation of nuclear resonant scattering data," *Hyperfine Interactions*, vol. 125, no. 1-4, pp. 149–172, 2000.

Chapter 2

EXPERIMENTAL METHODS

In this section, the experimental instrumentation and methods used to collect data that presented in my thesis is described.

2.1 Mössbauer Measurements

In the typical experimental setup for a conventional Mössbauer spectrometer in transmission geometry, as illustrated in Fig. 2.1, a Mössbauer source (^{57}Co embedded in a Rh matrix emitting 14.4 keV γ-rays as it decays to a metastable ^{57}Fe state) is mounted on an electromagnetic (EM) velocity Doppler drive (Wissel MDU-1200), along with a thin Fe-containing sample and a photon detector, all enclosed in lead shielding. A lead collimator is placed in front of the source to create a parallel beam of γ-rays. The EM velocity Doppler drive is operated in a mode of constant acceleration, usually at speeds ranging between 6 - 20 mm/s, set by a digital function generator (Wissel DFG-1200).

In transmission geometry, photons are allowed to travel straight from the driving end of the Doppler drive through the sample and into the detector. The detector used in the conventional Mössbauer spectrometer setup is a proportional counter or gas-filled detector containing a cylindrical Al tube, a 0.002-in Au-plated W wire as the anode, and a plexiglass window sealed with epoxy. The detector is filled with a 90%Ar-10%Methane gas mixture, flowed at a slow rate. Upon photon impact,

Ar atoms within the detector undergo ionization, and electrons are attracted to the anode wire, generating pulses proportional to the incident photon energy. These detector pulses are subsequently sorted according to height using a multi-channel analyzer, and a single channel analyzer is then used to count the 14.4 keV pulses, binning them in channels that are equally separated in time.

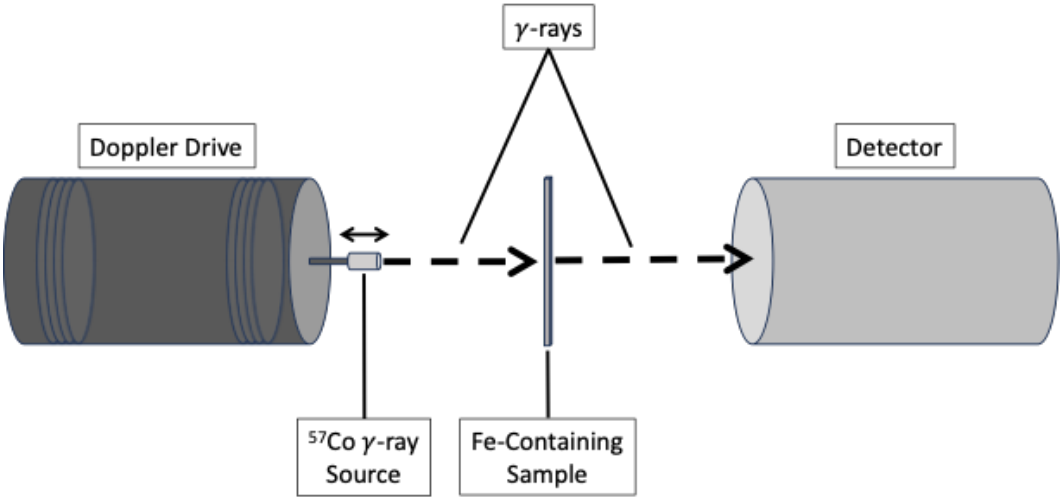

Figure 2.1: Electromagnetic Mössbauer spectrometer in transmission geometry.

The hyperfine structure of the resonant nuclei in a sample can be observed by conducting a scan of the incident γ-ray energy within the range of energy associated with the hyperfine splitting. As the sample is exposed to the motion of the γ-ray source, which moves back and forth at a speed with constant acceleration, the energy of the incident γ-rays is shifted due to the Doppler effect,

$$E = \frac{v}{c} E_\gamma \tag{2.1}$$

where v is the velocity of the source, c is the speed of light, and E_γ is the energy of the incident γ-rays (14.4 keV for 57-Fe). A Mössbauer spectrum is defined by the measured transmitted photons as the source velocity changes. In transmission

geometry, the dips with Lorentzian linewidths that are observed in the spectrum correspond to the resonant absorptions. The Mössbauer spectrum is defined by the transmitted photons that are measured as the source velocity undergoes oscillations. In transmission geometry, the dips observed in the spectrum, with Lorentzian linewidths, correspond to the resonant absorptions. Prior to the insertion of any Fe-containing samples into the Mössbauer spectrometer, a standard procedure includes the running of an alpha-Fe sample for calibration and conversion from channel to velocity.

2.2 High Pressure Measurements

All high-pressure synchrotron experiments were conducted using diamond-anvil cells (DACs). The applied force (F) per unit area (A) defines pressure (P):

$$P = \frac{F}{A} \tag{2.2}$$

Pressure can be increased by either applying more force or decreasing the area over which the force is applied. Diamond, due to its exceptional hardness and transparency to electromagnetic radiation, is capable of effectively generating high pressures. DACs have been reported to generate pressures as high as 750 GPa [1]. The fundamental concept of diamond-anvil cells involves arranging two diamonds to be pressed against each other. A schematic of the diamond configuration in a DAC is displayed in Fig. 2.2.

The flat diamond culet, with diameters typically ranging between 250μm-500μm, influences the applied pressure in the cell. Epoxy is used to secure the diamonds

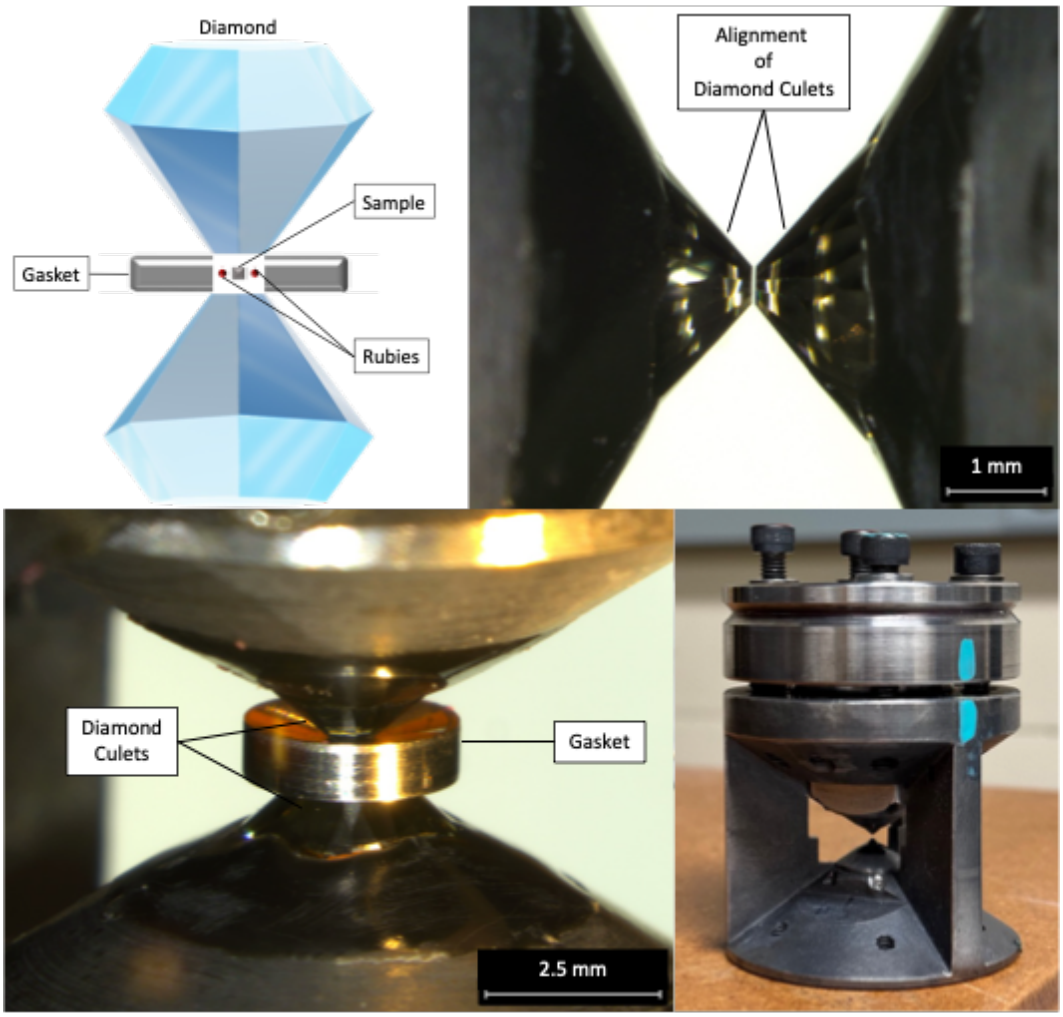

Figure 2.2: (Upper Left) Schematic representation of the diamonds and sample chamber. (Upper Right) Diamonds aligned in parallel. (Lower Left) The sample chamber enclosed by diamonds after loading the sample and rubies. (Lower Right) Panoramic-type diamond-anvil cell (DAC) used for high-pressure nuclear resonant inelastic X-ray scattering (NRIXS) and nuclear forward scattering (NFS) measurements.

on to tungsten carbide seats, which are then placed into the cell. The diamonds are aligned using set screws, ensuring both diamonds are centered, and their culets faces are parallel (refer to Fig. 2.2). This alignment helps prevent diamond breakage and gasket damage under high pressures. A metal gasket, pre-indented and laser-drilled [2] with a hole about 1/2 the culet diameter, serves as the sample chamber. It contains

a 50μm x 50μm square sample and a pair of rubies for monitoring pressure through optical fluorescence (as depicted in Fig. 2.3). Pressurized helium gas is used as the pressure medium in all high-pressure experiments to ensure hydrostatic pressure. Securing the cell involves tightening four screws with spring-loaded washers at the top, restraining the sample and rubies between the diamonds and gasket. The screws include pairs of left-handed and right-handed screws for sequential tightening and symmetrical compression of the cell.

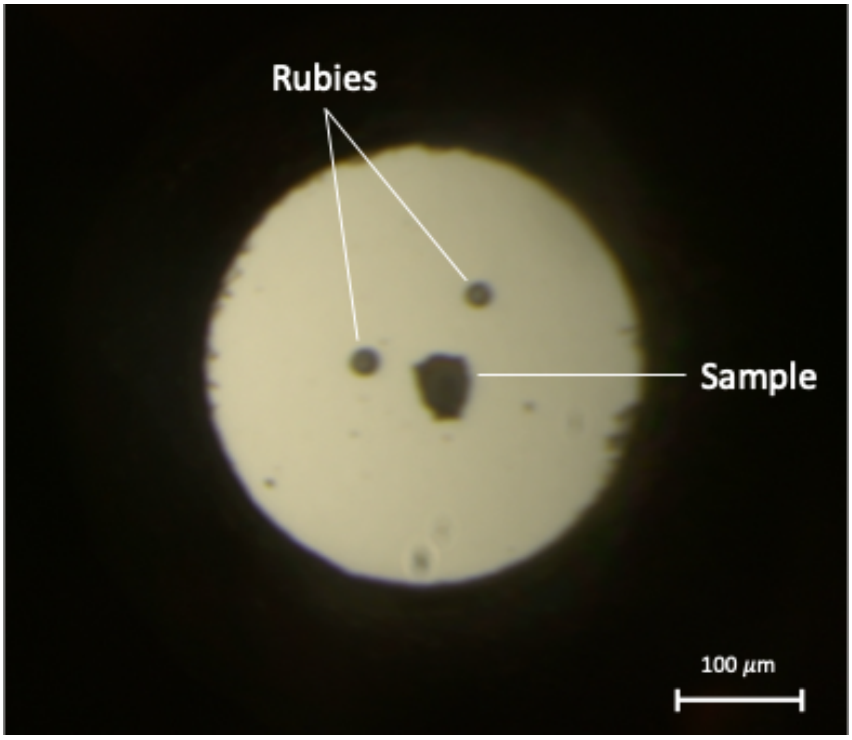

Figure 2.3: Close-up view of the sample chamber loaded with a 50um x 50um sample and two rubies.

High Pressure XRD High-pressure X-ray diffraction (XRD) experiments were conducted at beamline 16 ID-D of the Advanced Photon Source (APS). A symmetric-type DAC (see Fig. 2.4), featuring a wide-angle opening on the bottom side enabling

the observation of higher diffraction angles, was used for synchrotron XRD experiments. The creation of a sample chamber for all high-pressure XRD measurements

Figure 2.4: (Upper Left) Front view of the symmetric-type diamond-anvil cell (DAC). (Upper Right) Bottom view of the symmetric-type DAC displaying wide-angle opening. (Lower) Gas-membrane system used to make remote pressure changes.

involved the use of a rhenium gasket. Subsequently, a loaded and aligned DAC was mounted on a gas-membrane system, which allowed for remote and precise pressure adjustments. The key component of the gas-membrane system, as depicted in Fig. 2.4, is the ring-shaped bladder. For room temperature measurements, the DAC, along with the gas-membrane system, is directly placed on a motorized XYZ stage to help align the sample with the photon beam.

For experiments conducted under high temperature and high, the symmetric-type DAC is positioned within a furnace made of copper and is used in conjunction with a gas-membrane system. Temperature monitoring is enabled by the use of two thermocouples, with one fixed to the cell and another to the copper-block furnace. To maintain isolation from elevated temperatures, a water-cooled base connects the copper-block furnace to the motorized XYZ stage. The experimental setup, as illustrated in Figure 2.5 at beamline 16 ID-D, showcases the symmetric-type DAC within the copper-block furnace. Synchrotron XRD experiments in Chapter 4 utilized X-rays with an energy of 27 keV.

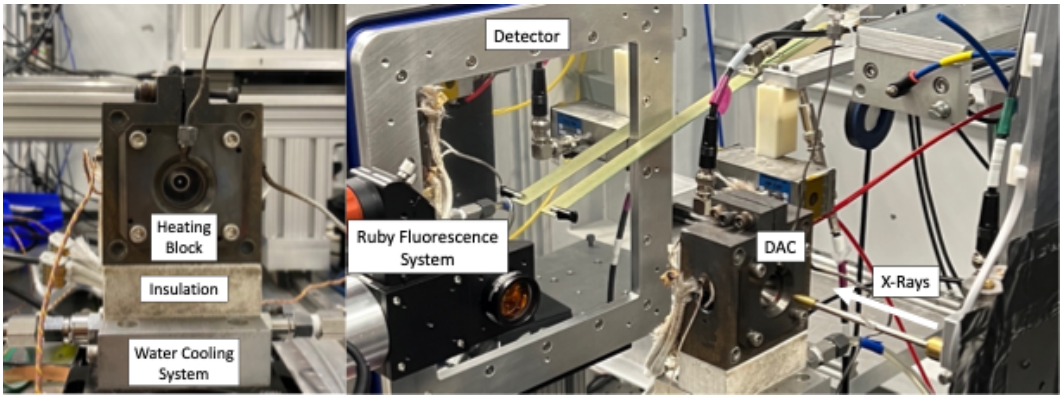

Figure 2.5: (Left) Copper-block furnace used for high temperature and high pressure experiments. (Right) Experimental configuration for high pressure X-ray diffraction (XRD) measurements at beamline 16 ID-D at the Advanced Photon Source (APS).

High Pressure NRIXS and NFS High-pressure nuclear resonance inelastic X-ray scattering (NRIXS) and nuclear forward scattering (NFS) experiments were conducted at beamline 3 ID-D of the Advanced Photon Source (APS). Synchrotron NRIXS and NFS measurements were performed using a panoramic-type DAC (refer to Fig. 2.2), featuring wide openings on the sides enabling the insertion of avalanche

photodiode detectors (APD). A beryllium gasket, transparent to X-rays, was used to establish a sample chamber for all high-pressure NRIXS and NFS measurements. Room temperature conditions were maintained for all NRIXS and NFS scattering measurements. In the case of NRIXS, three APD detectors were positioned as closely as possible to the sample through the side access of the panoramic-type DAC, optimizing the solid angle. Figure 2.6 illustrates a schematic representation of the APD configuration for NRIXS experiments. NFS measurements, on the other hand, were conducted in transmission geometry, requiring only one APD detector placed directly downstream in relation to the X-ray beam direction and subsequent to the DAC.

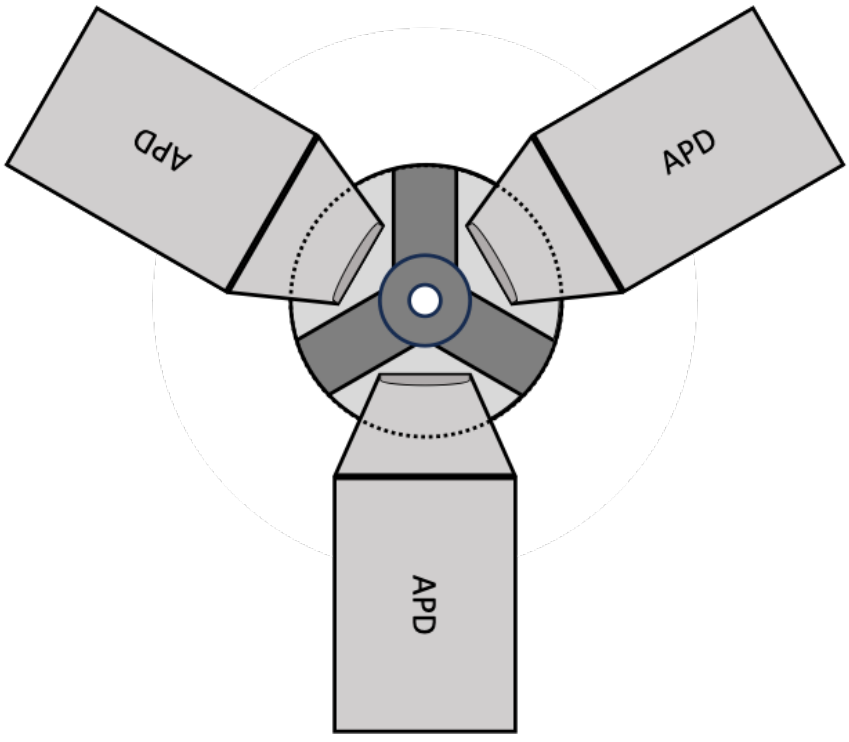

Figure 2.6: Top view schematic of the experimental setup of the panoramic diamond-anvil cell with avalanche photodiode detectors used for NRIXS measurements.

To ensure high-quality synchrotron measurements (XRD, NRIXS, NFS), time was

invested in searching for the gasket hole and identifying the sample by scanning the synchrotron X-ray beam. As pressure or temperature increased, the sample often shifted, necessitating rescanning of the synchrotron X-ray beam to locate the optimal sample position for signal maximization. For NRIXS and NFS measurements, pressure adjustment was achieved without a gas-membrane system, involving manual turning of the set of screws located at the top of the cell in pairs to symmetrically compress the DAC. The experimental configuration for NRIXS and NFS at beamline 3 ID-D is depicted in Fig. 2.7.

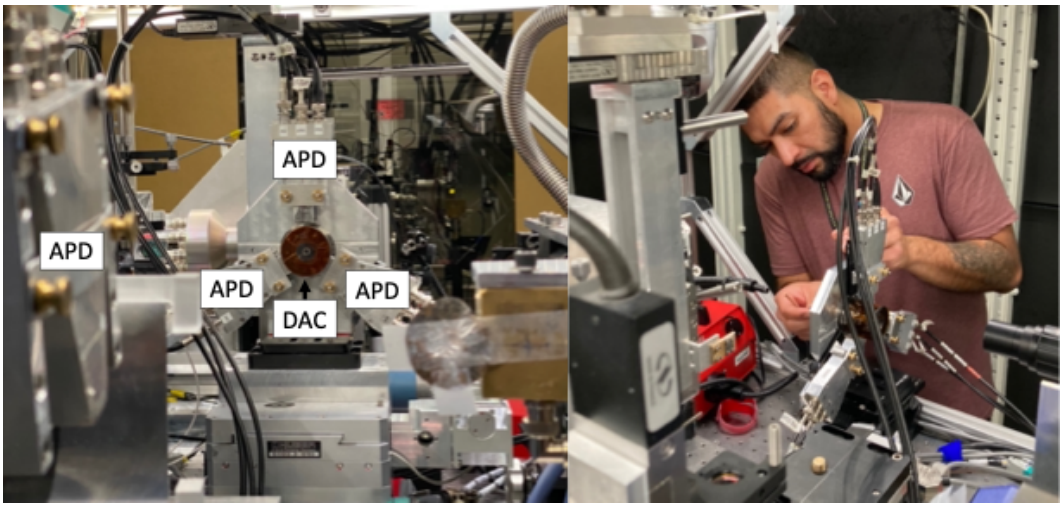

Figure 2.7: (Left) Experimental configuration for high pressure nuclear resonant inelastic X-ray scattering (NRIXS) and nuclear forward scattering (NFS) measurements at beamline 3 ID-D at the Advanced Photon Source (APS). (Right) Myself, Pedro Guzman, manually tuning the diamond-anvil cell (DAC) pressure.

References

[1] L. Dubrovinsky, N. Dubrovinskaia, E. Bykova, M. Bykov, V. Prakapenka, C. Prescher, K. Glazyrin, H.-P. Liermann, M. Hanfland, M. Ekholm *et al.*, "The most incompressible metal osmium at static pressures above 750 gigapascals," *Nature*, vol. 525, no. 7568, pp. 226–229, 2015.

[2] R. Hrubiak, S. Sinogeikin, E. Rod, and G. Shen, "The laser micro-machining system for diamond anvil cell experiments and general precision machining ap-

plications at the High Pressure Collaborative Access Team," *Review of Scientific Instruments*, vol. 86, no. 7, 2015.

Chapter 3

A MINIATURIZED PIEZOELECTRIC MÖSSBAUER SPECTROMETER WITH FEEDBACK CONTROL

3.1 Introduction

Mössbauer spectrometry is a robust technique that provides quantitative information about the structural, electronic, and magnetic properties of materials containing nuclear resonant isotopes such as ^{57}Fe, ^{119}Sn, ^{121}Sb, ^{151}Eu, or ^{191}Ir. The "Mössbauer effect" is based on the recoil-free emission and absorption of γ-rays in solids, allowing for the energy of the outgoing γ-ray to be accurate to 10^{-9} eV [1]. Mössbauer spectra provide quantifiable information on the interactions between the nucleus and its neighboring electrons, which cause small perturbations to the nuclear energy levels known as "hyperfine interactions". The energies of the γ-rays are tuned by moving the radiation source with a velocity, v, relative to the sample. This gives a Doppler shift $\Delta E = (v/c) \times E_0$, where E_0 is the energy of the γ-ray, approximately 14.41 keV for ^{57}Fe. This ΔE is scanned cyclically when acquiring a Mössbauer spectrum. A velocity range of ± 10 mm/s is sufficient to scan through many spectra of nuclear resonances for ^{57}Fe Mössbauer spectroscopy, however in some cases higher velocities are needed [1–4].

The main components of a standard Mössbauer spectrometer are an electromagnetic Doppler velocity drive, a source of γ-rays, and a photon detector [1, 4, 5]. A ^{57}Fe

Mössbauer spectrum is a plot of the intensity of detected 14.41-keV γ-ray photons versus Doppler velocity, v. The velocity transducer is a key element in a Mössbauer spectrometer since the quality of the spectrum is governed by the precise movement of the radiation source.

Miniaturized electromagnetic Doppler velocity drives were developed in the recent past for Mössbauer experiments on the surface of Mars [6, 7]. Notably, the MIMOS II was a miniature Mössbauer spectrometer built for missions on the Mars Exploration Rovers, Spirit and Opportunity. The MIMOS II spectrometer collected several Mössbauer spectra of rocks on Mars, and some spectra showed a significant amount of an iron oxyhydroxide, goethite (α-FeOOH). At the time, this was the best mineralogical evidence for presence of water on Mars, since goethite is formed only in an aqueous environment [8–10].

Compared to a miniature electromagnetic Doppler velocity drive, a piezoelectric actuator as a Doppler drive could significantly reduce the size, mass, and power requirements of a Mössbauer spectrometer, making Mössbauer spectrometry available for applications where miniaturization is essential. Previous publications report the use of piezoelectric actuators as Doppler velocity drives for Mössbauer spectrometry [11–15]. None, however, were operated with feedback control. Here we report the use of a mechanically-amplified, piezoelectric actuator as a Doppler velocity drive, both in open loop and in feedback-controlled configurations. Feedback control overcomes problems with thermal sensitivity of the piezoelectric material, and

successfully corrects for nonlinearities and parasitic oscillations in the dynamics of the drive. The system performance is nearly comparable to laboratory-based electromagnetic Doppler velocity drives.

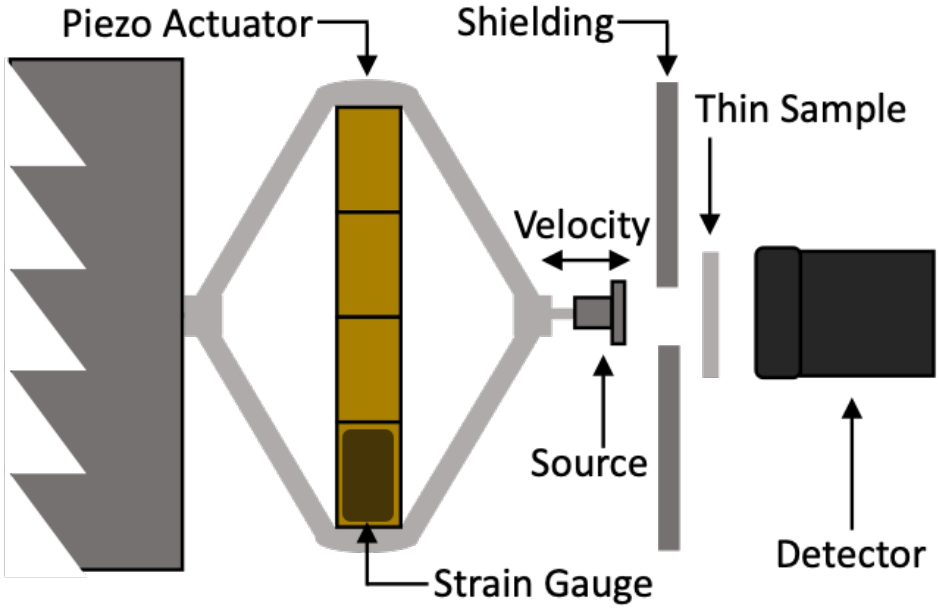

Figure 3.1: Spectrometer in transmission geometry. Radiation source is attached to mechanically-amplified piezoelectric actuator with velocity perpendicular to the thin sample absorber.

3.2 Experimental

Spectrometer Configuration

Fig. 3.1 shows a Mössbauer spectrometer with a piezoelectric Doppler velocity drive arranged in transmission geometry, where the distance between the source and the sample is 2 cm and the distance from the sample to the detector is 1 cm. The spectrometer includes a ^{57}Co source of γ-rays (Ritverc MCo7.162), with approximate activity of 2 mCi at the time of measurements, mounted on a mechanically-amplified piezoelectric actuator (Cedrat-Technologies APA1000L), a 30 μm thick

99.99+% purity α-iron foil as the absorbing sample, and a solid state detector (Ketek VITUS H50). A pair of 350 Ohm resistive strain gauges are used to monitor the displacement of the transducer and perform feedback control. The strain gauges have a T-Rosette design and are mounted directly on the multilayer actuator (MLA) by Cedrat-Technologies. The strain gauges are designed to be compatible with the Cedrat-Technologies piezoelectric controller (CCBu20).

The piezoelectric actuator with the γ-source undergoes cyclic displacements that follow a periodic reference waveform. Typically, Mössbauer spectrometers are operated in constant-acceleration mode, where the velocity follows a triangle wave. This linear velocity profile allows for evenly spaced velocity steps, and each time step corresponds to a channel in a multichannel scaler. A triangular velocity profile requires a quadratic displacement profile as the driving waveform for a piezoelectric Doppler velocity drive. The ^{57}Fe Mössbauer spectrum of α-iron contains six absorption lines due to the nuclear Zeeman effect [1, 16]. For each oscillation period, the Doppler shifted velocity passes through zero twice (at the turning points), giving two sets of six absorption lines as shown in Fig. 3.3. A microcontroller (Teensy 4.0) is used to generate the reference driving waveform with a lookup table. The reference waveform is input into the piezoelectric controller (CCBu20), which compares the feedback from the strain gauges to the reference waveform, and amplifies the signal to ultimately drive the piezoelectric actuator. Additionally, the microcontroller functions as a 2048 channel multichannel scaler for acquiring the

spectrum over many cycles of the Doppler drive.

The electronics in the experimental setup allow for determination of gamma energies with a sample-and-hold analog circuit combined with a voltage comparator for pulse detection. The microcontroller uses a 12-bit ADC for binning of the analog values. Figure 3.2 shows an energy spectrum collected with the microcontroller, where the pulses from the detector are sorted by their amplitude (energy binning). The software allows for user-inputted values to set the discriminator window, which is tested after each pulse is detected. The pulses in the window around 14.4 keV are then binned against velocity to obtain a Mössbauer spectrum.

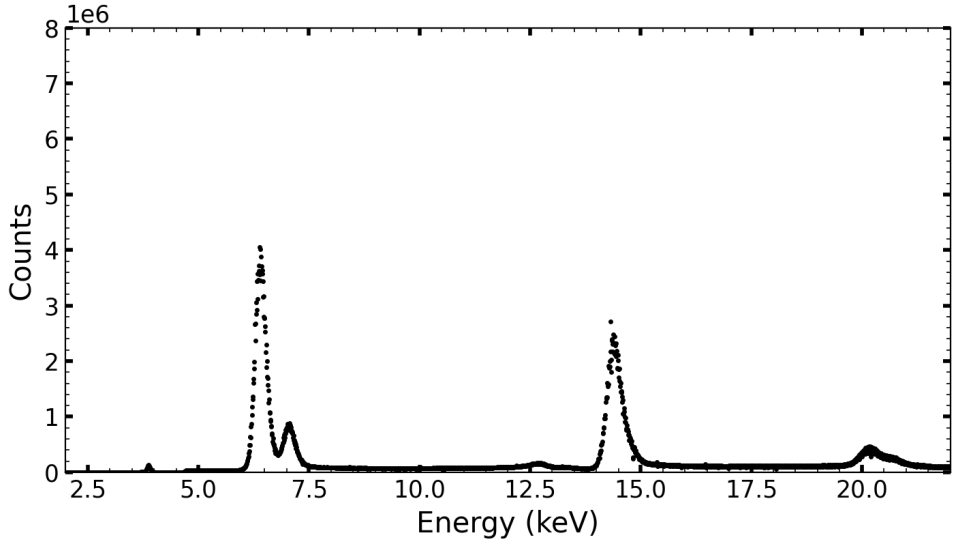

Figure 3.2: Energy spectrum resulting from the pulse-height-analysis (PHA) binning from the piezoelectric Mössbauer spectrometer.

Feedback Control and Low-Pass Filtering

^{57}Fe Mössbauer spectra collected without feedback control (i.e. open loop) were of poor quality, as shown in Fig. 3.3. For a high-performance spectrometer, feedback control of the piezoelectric actuator is required. The purpose of the PID controller is to diminish the error $e(t)$ between the strain gauge displacement signal $y(t)$ and the reference waveform $r(t)$ by adjusting the proportional (P), integral (I), and derivative (D) terms to generate a corrected drive signal, $d(t)$. The error is defined as:

$$e(t) = r(t) - y(t) \tag{3.1}$$

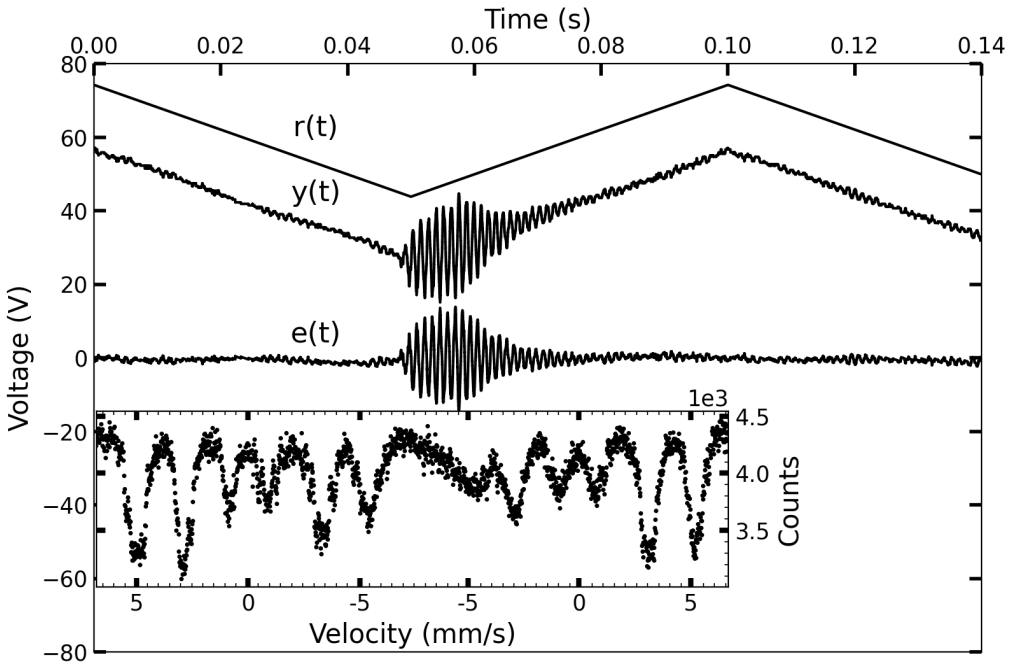

Figure 3.3: Open loop performance. Velocity error signal $e(t)$, measured LDV velocity profile $y(t)$, and reference velocity profile $r(t)$ at a driving frequency of 10 Hz. The measured LDV velocity profile $y(t)$ and the reference velocity profile $r(t)$ were offset from zero voltage. (Inset) ^{57}Fe Mössbauer measurements of a 30 μm α-iron foil collected at a driving frequency of 10Hz in open loop.

A digital PID controller operates with discrete time interval [17]. The CCBu20

controller provides digital PID control and a digital stabilizing filtering cell, in which ADC and DAC converters are used to sample the analog signals and perform the feedback control digitally. The sampling time of the digitization process, T, determines the discrete time events $t = nT$ (where $n = 0, 1, 2,...$). The adjustment on the drive signal $d(t)$ by the proportional term is:

$$d_P(t) = k_P\, e(nT) \tag{3.2}$$

providing direct amplification by the proportional gain k_P. The adjustment on the drive signal by the integral term is:

$$d_I(t) = \frac{T}{T_I} \sum_{m=1}^{n} e(mT) \tag{3.3}$$

where T_I is the integration time. Over time, the integral term minimizes deviation from the average reference value. The adjustment on the drive signal by the derivative term is:

$$d_D(t) = T_D \frac{e(nT) - e((n-1)T)}{T} \tag{3.4}$$

where T_D is the derivative time constant. The derivative term impacts the stability properties of the feedback control by preventing overshoot. The overall adjustment on the drive signal by all three components is [17–19]:

$$\begin{aligned} d_{PID}(t) &= k_P \Big[e(nT) + \frac{T}{T_I} \sum_{m=1}^{n} e(mT) \\ &+ \frac{T_D}{T} [e(nT) - e((n-1)T)] \Big] \end{aligned} \tag{3.5}$$

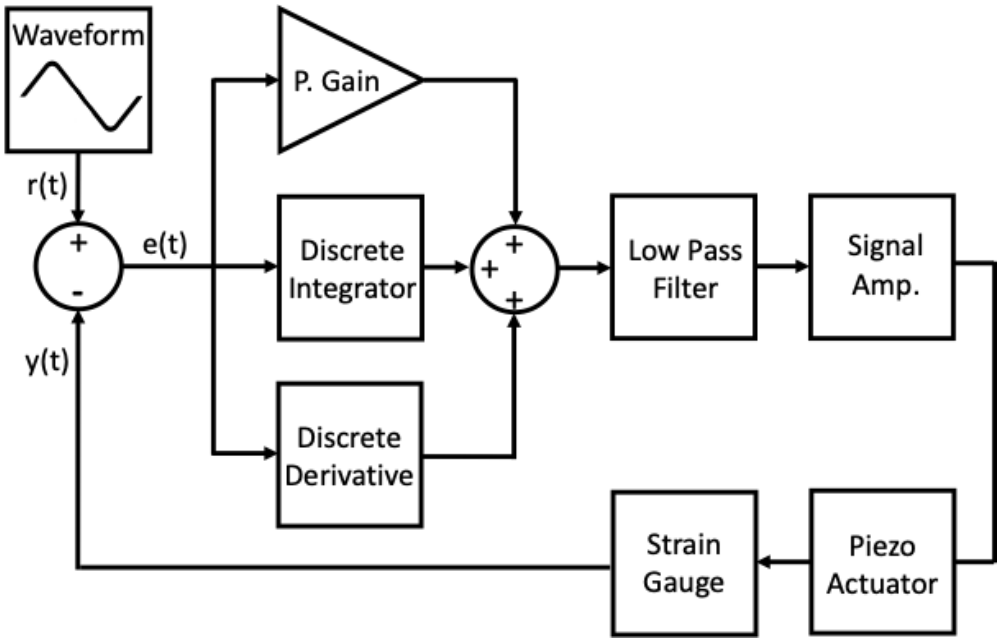

Figure 3.4: Schematic of basic digital control loop.

Feedback control enables the piezoelectric actuator to reduce error, $e(t)$, in position, and therefore its velocity. The PID parameters influence the response speed of the controller but also introduce energy into system resonant modes, which degrade performance. A low-pass filter was placed in line with the feedback controller to limit the impact of the resonant frequency modes of the actuator [20]. Fig. 3.4 is a schematic block diagram illustrating the digital PID controller and filter.

Laser Doppler Vibrometer

Single-point laser Doppler vibrometer (LDV) measurements were performed with a Polytec OFV-3001 vibrometer to monitor the velocity profile of the piezoelectric Doppler velocity drive. LDV is a non-contact technique for probing vibrations of a surface. During an LDV measurement, a beam from a laser (f_0) is split into a test and reference beam. A Bragg cell adds a frequency shift (f_b) to the test

beam that is directed to the target (piezoelectric actuator). The motion of the target adds a Doppler shift frequency to the beam given by: $f_d = 2v(t)/\lambda$, where λ is the wavelength of the beam and $v(t)$ is the velocity of the target. The resulting frequency of the beam measured at the detector is a frequency modulated signal $f_{mod} = f_b + 2v(t)/\lambda$, from which the velocity vs. time is obtained [21, 22].

Mössbauer Data Fit

The velocity scale is calibrated with the known hyperfine magnetic field splitting of α-iron to convert from channel number to velocity (mm/s) [23]. Using the Mössbauer fitting program Fit;o) [24], we fit our data with a sextet having Lorentzian profiles, as shown in Fig. 3.5. The obtained hyperfine parameters were 33 T for the hyperfine magnetic field and the isomer shift is set to zero since the sample is our reference absorber. Relative areas of 3:2.5:1:1:2.5:3 for peaks (1,6), (2,5), (3,4) were obtained from the fit. The average the full-width-at-half-maximum (FWHM) for peaks (1,6), (2,5), (3,4) were 0.348 mm/s, 0.316 mm/s, and 0.245 mm/s respectively. The chi-square value, which describes the quality of model fit for data of a particular statistical quality, was 8.6 for the fit of Fig. 3.5.

An isotropic distribution of hyperfine magnetic fields in α-iron gives a 3:2:1:1:2:3 relative area ratio for peaks (1,6), (2,5), (3,4). The magnetic dipole transitions in ^{57}Fe have radiation patterns that go as $(1 + \cos^2(\theta))$ if there is a change in z-component of angular momentum of ± 1, and as $\sin^2(\theta)$ if this change is 0. Here (θ) is the angle between the path of the γ-ray and the z-axis of the hyperfine magnetic field. When $\theta = 90°$, so the magnetization is in the plane of the foil sample, the ratio becomes

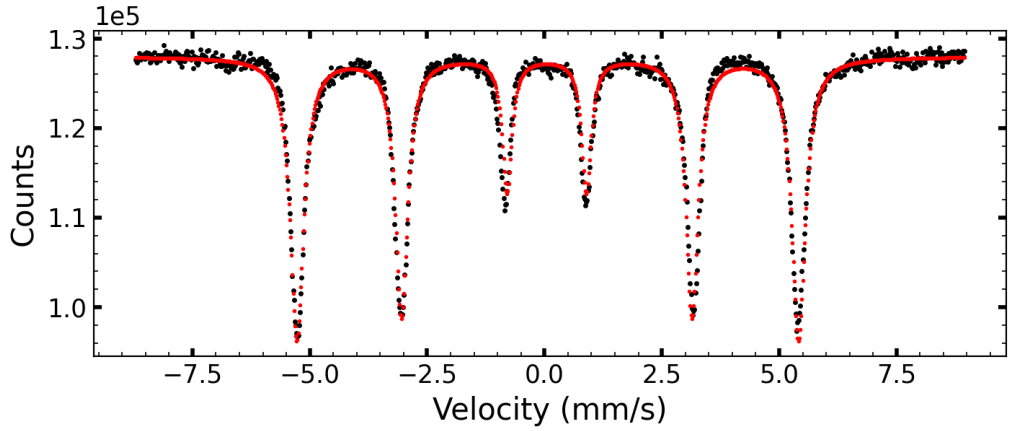

Figure 3.5: ^{57}Fe Mössbauer spectrum of a 30 μm α-iron foil (black) collected with the piezoelectric Doppler velocity drive at a driving frequency of 10 Hz, a 100 V DC offset, 70 Hz Low Pass Filter, and in closed loop. Fit;o) sextet fit with Lorentzian profiles (red).

3:4:1:1:4:3 [25]. Magnetic texture is common in foil samples of iron, and there is a slight texture for the sample of Fig. 3.5.

Mössbauer Velocity Ranges

Our piezoelectric drive system is capable of achieving a wide range of velocities by tuning the amplitude of the driving voltage and tuning the driving frequency (the resulting velocity is dependent on both parameters). Figure 3.6 shows Mössbauer spectra of alpha-iron with a variety of velocity ranges achieved by increasing the amplitude of the driving voltage.

3.3 Results

In open loop operation (without feedback control), Fig. 3.3 shows a number of peak distortions and broadenings of the six peaks from α-iron. Also shown is a mechanical resonance in the error signal $e(t)$ near –6 mm/s. This originated with

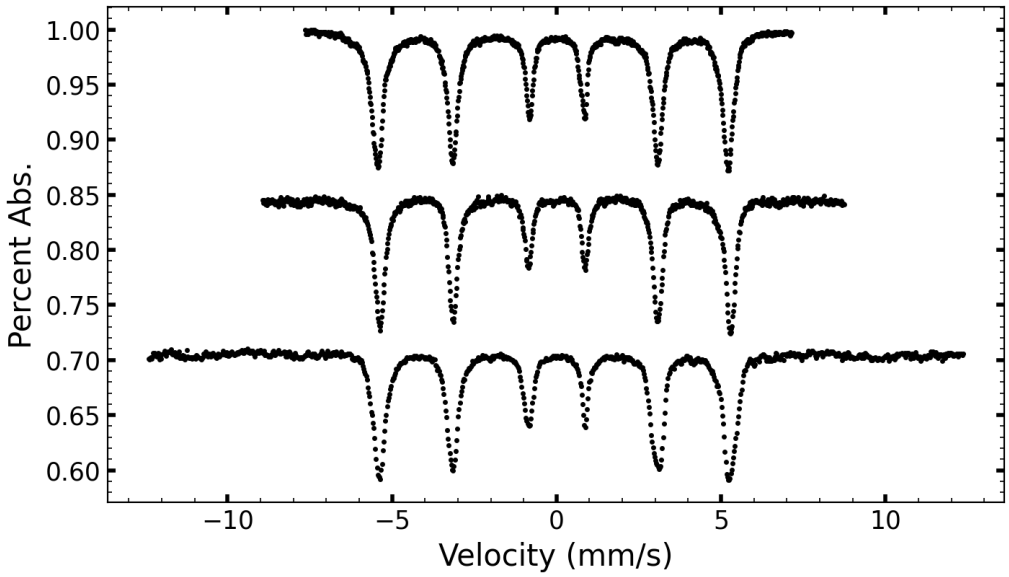

Figure 3.6: Closed loop performance at different velocity ranges. ^{57}Fe Mössbauer measurements of a 30 μm α-iron foil collected at a driving frequency of 10Hz, a 100 V DC offset, 70 Hz Low Pass Filter, and in closed loop. (Top) Driving voltage amplitude of 40 V, (Middle) driving voltage amplitude of 48 V, and (Bottom) driving voltage amplitude of 56 V.

the stack of piezoelectric elements becoming loose at the corresponding extension. This problem was minimized by applying a DC offset to the drive signal to keep the piezoelectric stacks in a state of expansion. This DC bias was used for closed loop, too. The feedback-controlled piezoelectric Doppler velocity drive was optimized by tuning the PID parameters and measuring the velocity profile $y(t)$ with the LDV. A sinusoidal transition at the maxima of the velocity profile $y(t)$ was implemented by customizing the reference waveform. The smoothed reversals in acceleration suppress the jerk at the velocity maxima.

The tuned piezoelectric Doppler drive system in closed loop shows only minimal peak distortions in the measured ^{57}Fe Mössbuaer spectrum of α-iron, as shown in Fig. 3.7. The spectrum of the 30 μm α-iron foil collected with the piezoelectric

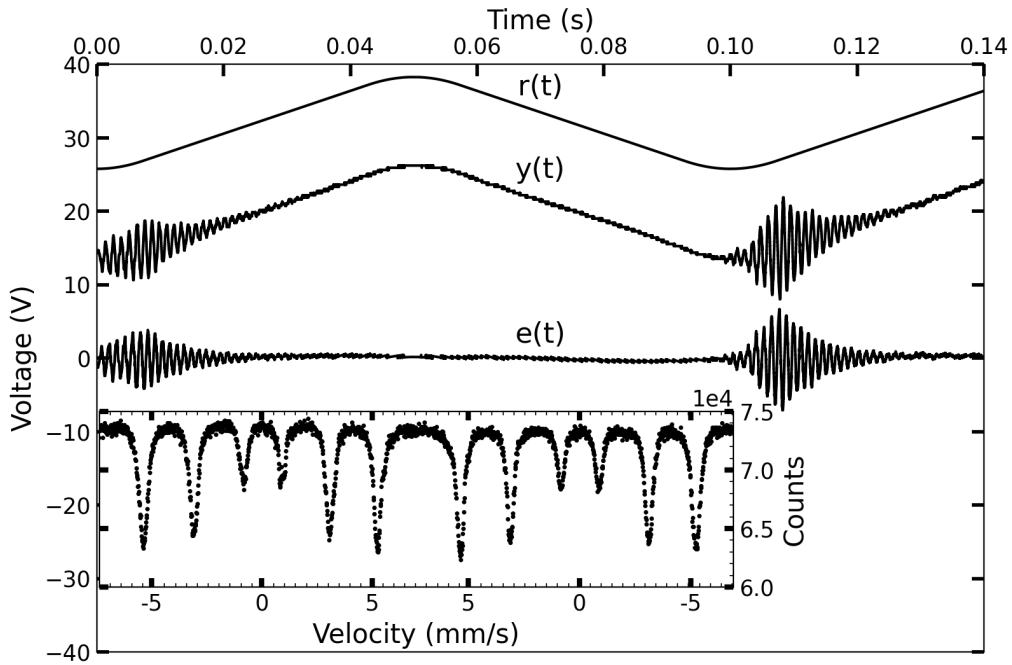

Figure 3.7: Closed loop performance. Velocity error signal $e(t)$, measured LDV velocity profile $y(t)$, and reference velocity profile $r(t)$ at a driving frequency of 10Hz, 30 V DC offset, and 70 Hz Low Pass Filter. The measured LDV velocity profile $y(t)$ and the reference velocity profile $r(t)$ were offset from zero voltage. (Inset) ^{57}Fe Mössbauer measurements of a 30 μm α-iron foil collected at a driving frequency of 10Hz, a 30 V DC offset, 70 Hz Low Pass Filter, and in closed loop.

Doppler drive is compared to the spectrum of the same α-iron absorber collected with a conventional electromagnetic drive (Wissel MVT-1000, DFG-1200, MDU-1200) in Fig. 3.8. The α-iron spectrum was first fit to six Lorentzian lines with unconstrained centers, widths, and heights. The linearity of our piezoelectric Doppler drive is quantified by comparing the separations in velocity of the Mössbauer peaks (1,2), (2,3), (4,5), (5,6) for α-iron, which should be equal from the systematics of the nuclear Zeeman effect. Table I shows that the variations in these peak separations, an indicator of the linearity of the drive, were within 3.5 percent. This could be corrected by adapting the reference waveform, $r(t)$. Table II shows that the full-width-at-half-maximum (FWHM) of the Mössbauer peaks obtained with

our piezoelectric Doppler velocity drive is comparable to the peaks obtained with the conventional electromagnetic drive. Six Lorentzian lines were fit to the α-iron spectrum with the program Fit;o) [24], and gave an average FWHM that was 10 percent less than the results in Table II. There are, however, slight distortions in the peaks that were sensitive to the parameters of the PID controller. These distortions may be a limitation of performing feedback control with a strain gauge attached to the piezoelectric stack, which is not in contact with the radiation source.

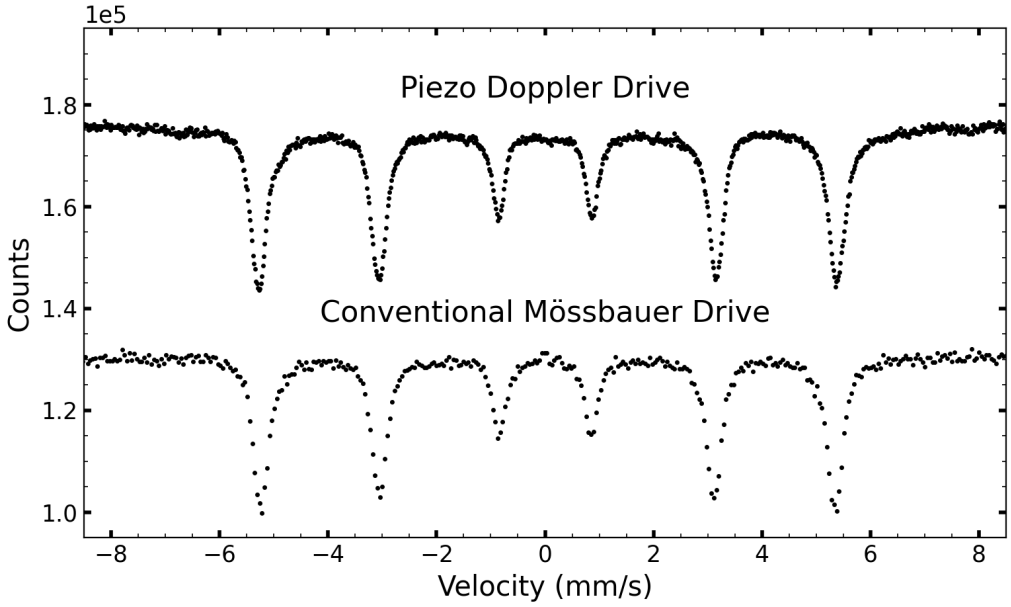

Figure 3.8: Piezoelectric system with feedback control results in spectra comparable to conventional system. (Top) ^{57}Fe Mössbauer spectrum of a 30 μm α-iron foil collected with the piezoelectric Doppler velocity drive at a driving frequency of 10 Hz, a 100 V DC offset, 70 Hz Low Pass Filter, and in closed loop. (Bottom) ^{57}Fe Mössbauer spectrum of the same 30 μm α-iron foil collected with electromagnetic Doppler velocity drive.

3.4 Discussion

Piezoelectric materials exhibit an inherent hysteresis [26, 27], that gives a non-linear response to the driving voltage. Without feedback control, the performance of our

Table 3.1: Linearity comparison between piezoelectric Doppler drive and electromagnetic Doppler drive.

Peak Separation	Piezoelectric Drive (mm/s)	Electromagnetic Drive (mm/s)
1-2	2.211	2.249
2-3	2.203	2.278
4-5	2.283	2.224
5-6	2.232	2.198

Table 3.2: Peak width comparison between piezoelectric Doppler drive and electromagnetic Doppler drive.

Peak No.	Piezoelectric Drive FWHM (mm/s)	Electromagnetic Drive FWHM (mm/s)
1	0.343	0.338
2	0.337	0.319
3	0.267	0.261
4	0.273	0.270
5	0.321	0.322
6	0.364	0.331

piezoelectric Doppler velocity drive was comparable to that of previous reports [11–15]. Feedback control is the main advantage of our piezoelectric Doppler velocity drive over those in previous reports because it overcomes the inherent dimensional hysteresis of the piezoelectric material. Feedback control is known to enhance the accuracy in positioning, and is necessary to achieve precision positioning of piezoelectric actuators [28, 29]. Additionally, it allows for the system to correct for changes in temperature, as the properties of piezoelectric materials are temperature dependent. Cedrat-Technologies specifies an accuracy in position of 49 nm for their mechanically-amplified piezoelectric actuator (APA1000L) [30]. Precise positioning, low operating voltage, large displacement, and fast response time of amplified piezoelectric actuators make them suitable in a wide range of applications [31–34]. The present work demonstrates that precision velocities are also possible, at least

in the range needed for ^{57}Fe Mössbauer spectrometry, typically ±10 mm/s or smaller.

A mechanically-amplified piezoelectric actuator offers a significant reduction in mass as a Mössbauer Doppler velocity drive. For comparison, the mass of a conventional Mössbauer velocity transducer (Wissel MVT-1000) is 4.5 kg. The mass of a piezoelectric actuator (APA1000L) is 0.19 kg, a reduction of a factor of 20. The mass can be reduced further by a factor of 100 with the use of a lightweight piezoelectric bender actuator (1.7 g). A bender actuator is currently being investigated, but it presents challenges with torsional modes in its dynamics. Such a large reduction in mass opens the possibility for the development of an ultraminiature lightweight Mössbauer spectrometer. Due to the abundance of iron in our solar system, an ultraminiature lightweight Mössbauer spectrometer is an ideal instrument for investigating the lunar and Martian surfaces. Additionally, piezoelectric actuators can operate in high radiation environments and have been qualified for up to 100 krad levels [35].

The main benefits of lower mass and size are applicability and cost. A piezoelectric drive can be useful for scientific payloads for space missions that are limited by size, mass, and power. Cryogenic measurements with ^{191}Ir or other cold radiation sources may be easier with this smaller drive. Finally, a low-cost ^{57}Fe Mössbuaer spectrometer could serve as an instrument for an undergraduate lab class.

3.5 Conclusion

The design and optimization of a piezoelectric actuator with feedback control as a velocity transducer for ^{57}Fe Mössbauer spectrometry is reported. The performance of the prototype piezoelectric Doppler velocity drive with a PID controller is nearly identical to a conventional electromagnetic Doppler velocity drive, and further improvements are possible. Compared to electromagnetic drives, piezoelectric actuators have significantly reduced size, mass, and cost.

References

[1] B. Fultz, "Mössbauer Spectrometry," *in Characterization of Materials, E. Kaufmann, Ed.*, pp. 1–21, Wiley, 2012.

[2] H. Lustig, "The Mössbauer effect," *American Journal of Physics*, vol. 29, no. 1, pp. 1–18, 1961.

[3] D. O'Connor, "The Mössbauer effect," *Contemporary Physics*, vol. 9, no. 6, pp. 521–535, 1968.

[4] G. K. Wertheim, "Mössbauer effect," *Physics Today*, vol. 20, no. 7, pp. 31–37, 1967.

[5] T. Cranshaw, "Mössbauer spectroscopy," *Journal of Physics E: Scientific Instruments*, vol. 7, no. 7, p. 497, 1974.

[6] E. Kankeleit, J. Foh, P. Held, G. Klingelhöfer, and R. Teucher, "A Mössbauer experiment on Mars," *Hyperfine Interactions*, vol. 90, pp. 107–120, 1994.

[7] G. Klingelhoefer, R. V. Morris, B. Bernhardt, D. Rodionov, P. A. de Souza, S. W. Squyres, J. Foh, E. Kankeleit, U. Bonnes, R. Gellert *et al.*, "Athena MIMOS II Mössbauer spectrometer investigation," *Journal of Geophysical Research: Planets*, vol. 108, no. E12, p. 8067, 2003.

[8] G. Klingelhoefer, E. DeGrave, R. V. Morris, A. Van Alboom, V. G. de Resende, P. De Souza, D. Rodionov, C. Schröder, D. W. Ming, and A. Yen, "Mössbauer spectroscopy on Mars: goethite in the Columbia Hills at Gusev crater," *Hyperfine Interactions*, vol. 166, pp. 549–554, 2005.

[9] G. Klingelhöfer, D. Rodionov, R. Morris, C. Schröder, P. deSouza, D. Ming, A. Yen, B. Bernhardt, F. Renz, and I. Fleischer, "MIMOS II on MER One

Year of Mossbauer Spectroscopy on the Surface of Mars: From Jarosite at Meridiani Planum to Goethite at Gusev Crater," *Lunar and Planetary Science XXXVI, Part 11*, p. 2349, 2005.

[10] R. V. Morris, G. Klingelhoefer, C. Schröder, D. S. Rodionov, A. Yen, D. W. Ming, P. A. de Souza, I. Fleischer, T. Wdowiak, R. Gellert *et al.*, "Mössbauer mineralogy of rock, soil, and dust at Gusev crater, Mars: Spirit's journey through weakly altered olivine basalt on the plains and pervasively altered basalt in the Columbia Hills," *Journal of Geophysical Research: Planets*, vol. 111, p. E02S13, 2006.

[11] R. Gerson and W. S. Denno, "Mössbauer Spectrometer using a Piezoelectric Bar in Resonant Oscillation," *Review of Scientific Instruments*, vol. 36, no. 9, pp. 1344–1346, 1965.

[12] K. Schmidt, C. Dierieck, J. Lafaut, E. Vermeulen, and M. Elskens, "Description of a Mössbauer spectrometer using a piezoelectric bar," *Nuclear Instruments and Methods*, vol. 81, no. 1, pp. 211–213, 1970.

[13] K. Schmidt, M. Huyse, J. De Raedt, G. Langouche, M. Van Rossum, and R. Coussement, "A computerized piezoelectric Mössbauer spectrometer," *Nuclear Instruments and Methods*, vol. 120, no. 2, pp. 287–291, 1974.

[14] N. Sakai, "A new Mössbauer transducer using piezoelectric bimorph actuators," *Hyperfine Interactions*, vol. 42, no. 1, pp. 1165–1168, 1988.

[15] L. Casas, E. Molins, and A. Roig, "Miniaturization of a Mössbauer spectrometer using a piezotransducer and a solid state detector," *Hyperfine interactions*, vol. 141, no. 1, pp. 125–129, 2002.

[16] P. Gütlich, E. Bill, A. X. Trautwein, and S. Mørup, *Hyperfine Interactions. In: Mössbauer Spectroscopy and Transition Metal Chemistry*. Springer, 2011.

[17] P. Kohout, L. Kouřil, J. Navařík, P. Novák, and J. Pechoušek, "Optimized linear motor and digital PID controller setup used in Mössbauer spectrometer," in *AIP Conference Proceedings*, vol. 1622. American Institute of Physics, 2014, pp. 50–57.

[18] J. Balátě, *Automatic Control*. BEN - Technical Literature, 2004.

[19] M. Kocur, S. Kozak, and B. Dvorscak, "Design and implementation of FPGA-digital based PID controller," in *Proceedings of the 2014 15th International Carpathian Control Conference (ICCC)*. IEEE, 2014, pp. 233–236.

[20] Cedrat-Technologies, *UC45 Product and Warranty Information.*, 9 2012. [Online]. Available: https://www.cedrat-technologies.com/fileadmin/user_upload/CTEC/Mechatronic_products/User_s_manual/Inst_Man_UC45_v14_NEW.pdf

[21] Polytec GmbH, *User Manual Laser Doppler Vibrometer*, 1996.

[22] E. P. Tomasini and P. Castellini, *Laser Doppler Vibrometry*. Springer, 2020.

[23] R. Preston, S. Hanna, and J. Heberle, "Mössbauer effect in metallic iron," *Physical Review*, vol. 128, no. 5, p. 2207, 1962.

[24] J. í Hjøllum and M. B. Madsen, "Fit;o) – A Mössbauer spectrum fitting program," *arXiv preprint arXiv:0912.0449*, vol. 1, 2009.

[25] F. J. Berry and D. P. Dickson, *Mössbauer Spectroscopy*. Cambridge University Press Cambridge, 1986.

[26] D. Damjanovic, "Hysteresis in piezoelectric and ferroelectric materials," *The Science of Hysteresis*, vol. 3, pp. 337–456, 2006.

[27] R. Changhai and S. Lining, "Hysteresis and creep compensation for piezoelectric actuator in open-loop operation," *Sensors and Actuators A: Physical*, vol. 122, no. 1, pp. 124–130, 2005.

[28] J. Gan and X. Zhang, "A review of nonlinear hysteresis modeling and control of piezoelectric actuators," *AIP Advances*, vol. 9, no. 4, p. 040702, 2019.

[29] Z. Chi and Q. Xu, "Recent advances in the control of piezoelectric actuators," *International Journal of Advanced Robotic Systems*, vol. 11, no. 11, p. 182, 2014.

[30] Cedrat-Technologies, *APA1000L Technical Data Sheet.*, 6 2022. [Online]. Available: https://cedrat-technologies.com/wp-content/uploads/2023/03/APA1000L-1.pdf

[31] R. Le Letty, F. Claeyssen, N. Lhermet, and P. Bouchilloux, "New amplified piezoelectric actuator for precision positioning and active damping," in *Smart Structures and Materials 1997: Smart Structures and Integrated Systems*, vol. 3041. SPIE, 1997, pp. 496–504.

[32] F. Claeyssen, R. Le Letty, E. F. Barillot, E. N. Lhermet, and E. G. Rajeev, "Amplified Piezoelectric Actuators for Air & Space Applications," *Cedrat Technologies SA, ZIRST*, vol. 38246, 2003.

[33] P. Bouchilloux, F. Claeyssen, and R. Le Letty, "Amplified piezoelectric actuators: from aerospace to underwater applications," *Smart Structures and Materials 2004: Industrial and Commercial Applications of Smart Structures Technologies*, vol. 5388, pp. 143–154, 2004.

[34] M. Ragonet, J. Petiniot, M. Fournier, T. Porchez, O. Sosnicki, and C. Bouchet, "Potentialities of APA Composite Shell Actuators and SA75D Amplifier for New Dynamic Applications," in *Proceedings of the 15th International Conference on New Actuators, Bremen, Germany*, 2016, pp. 13–15.

[35] Cedrat-Technologies, *Piezoelectric Actuators Product and Warranty Information.*, 11 2016. [Online]. Available: https://cedrat-technologies.com/wp-content/uploads/2023/07/inst_man_actuator_v6.1.pdf

Chapter 4

THE PRESSURE INDUCED INVAR EFFECT IN $FE_{55}NI_{45}$: AN EXPERIMENTAL STUDY WITH NUCLEAR RESONANT SCATTERING

4.1 Introduction

Invar effect

The fcc alloy $Fe_{64}Ni_{36}$ exhibits the classic Invar effect, where its thermal expansion is nearly zero at ambient conditions. In 1920, Charles-Édouard Guillaume was awarded the Nobel Prize "in recognition of the service he has rendered to precision measurements in Physics by his discovery of anomalies in nickel steel alloys." [1–3]. Invar alloys of $Fe_{64}Ni_{36}$ have long been used for precision instruments and devices that maintain their dimensional stability over a range of temperatures [4].

Guillaume found that the Invar effect was lost for non-magnetic states of the material, and understood that there was a role for magnetism in thermal expansion to counteract the expected positive thermal expansion of the alloy. Recently, the phonon and magnetic contributions to thermal expansion in Invar were isolated, and shown to cancel [5]. Furthermore, interactions between spins and phonons were shown to extend the range of pressures for near-zero thermal expansion in $Fe_{65}Ni_{35}$ from 0 to 3 GPa (the Curie pressure was reported to be 4.6 GPa). Invar behavior has been reported in other systems such as Fe-Pt, Fe-Co, Ni-Mn and hcp Gd [6–14]. Many amorphous materials containing iron show Invar anomalies at ambient pres-

sure. Ref. [4, 15–19] provides a thorough review of experimental and theoretical work on the Invar problem.

Both lattice dynamics and magnetism are changed with pressure. Under pressure, it was reported that Invar behavior develops in $Fe_{55}Ni_{45}$, $Fe_{20}Ni_{80}$, and Pd_3Fe [20–22], and effects of pressure on materials with the ambient Invar effect have been investigated in numerous previous studies [23–40].

Here we present a study of the pressure-induced Invar effect in $Fe_{55}Ni_{45}$, first reported in 2001 [20]. By comparing X-ray lattice parameters from samples in a diamond-anvil cell at two temperatures, we found an anomalous thermal expansion occurring at pressures between 7 and 13 GPa. Nuclear forward scattering (NFS) showed that a Curie transition in $Fe_{55}Ni_{45}$ occurs at 13 GPa, so there should be an increase in spin disorder and magnetic entropy just below this pressure. Nuclear resonant inelastic X-ray scattering (NRIXS) was used to measure the phonon density of states (DOS) of ^{57}Fe atoms. The NRIXS spectra showed an arrest in the increase of longitudinal phonon modes between 7 and 13 GPa, but the average phonon entropy decreased as the frequencies of other phonons increased with pressure. The decrease of phonon entropy counteracted precisely the pressure-dependence of the magnetic entropy, which increased from spin disorder as the Curie transition was approached. A Maxwell relation shows that magnetism and phonons therefore have cancelling contributions to thermal expansion near 10 GPa. The behavior is similar to what was observed below the Curie pressure in $Fe_{65}Ni_{35}$ [5] at pressures to 3 GPa. The arrest of the longitudinal phonon frequencies is interpreted as evidence

of spin-phonon interactions.

Thermophysics of Thermal Expansion

The fractional change in volume V with temperature T is the volume coefficient of thermal expansion, β:

$$\beta = \frac{1}{V}\left(\frac{\partial V}{\partial T}\right)_{\mathrm{P}} \tag{4.1}$$

The phonon and spin contributions to the thermal expansion can be found experimentally by use of a thermodynamic Maxwell relation [5]

$$\left(\frac{\partial V}{\partial T}\right)_{\mathrm{P}} = -\left(\frac{\partial S}{\partial P}\right)_{\mathrm{T}}, \tag{4.2}$$

so β can expressed as

$$\beta = -\frac{1}{V}\left(\frac{\partial S}{\partial P}\right)_{\mathrm{T}} \tag{4.3}$$

The entropy is dominated by vibrational and magnetic degrees of freedom. (The pressure dependence of the electronic contribution was found to be negligible [5].)

$$\beta = -\frac{1}{V}\left[\left(\frac{\partial S_{\mathrm{ph}}}{\partial P}\right)_{\mathrm{T}} + \left(\frac{\partial S_{\mathrm{mag}}}{\partial P}\right)_{\mathrm{T}}\right] \tag{4.4}$$

The contribution of phonons is measured through nuclear resonant inelastic X-ray scattering (NRIXS), while the contribution of spins is measured through nuclear forward scattering (NFS).

Elinvar Effect

In additon to the Invar effect, Charles-Édouard Guillaume discovered that the elastic modulus had little variation with temperature for fcc alloys of $Fe_{55}Ni_{45}$ [1–3].

These alloys, named "Elinvar," are used in many applications requiring elastic stability over a broad range of temperatures, such as springs and tuning forks [4]. For most materials, elastic constants generally decrease with temperature owing to vibrational anharmonicity, and such a contribution is expected in Elinvar, too. The elastic stability of Elinvar with temperature may be caused by an opposing effect from the change of magnetism with temperature, but there is no universal agreement on the fundamental mechanism responsible for the Elinvar effect.

Thermophysics of Bulk Modulus

The pressure is the response of the free energy to a change in volume

$$P = \left(\frac{\partial F}{\partial V}\right)_T \tag{4.5}$$

Equation 4.5 gives a thermodynamic relation for the bulk modulus of Eq. 4.12 by using the Helmholtz free energy $F = U - TS$

$$B_T = V\left(\frac{\partial^2 F}{\partial V^2}\right)_T \tag{4.6}$$

$$B_T = V\left(\frac{\partial^2 U}{\partial V^2}\right)_T - VT\left(\frac{\partial^2 S}{\partial V^2}\right)_T \tag{4.7}$$

where U is the internal energy, T is temperature, and S is entropy. The B_T should be the same for either positive or negative changes in V, if the changes are small.

The temperature derivative of Eq. 4.7 gives the temperature dependence of the bulk modulus. The first term on the right-hand-side does not depend on temperature, so

$$\frac{\partial B_T}{\partial T} = -V\left(\frac{\partial^2 S}{\partial V^2}\right)_T \tag{4.8}$$

We show that the Elinvar behavior occurs at low pressures, but the NRIXS and NFS measurements were not sufficiently precise to pinpoint its thermodynamic origins.

4.2 Experimental

Sample preparation

The $Fe_{55}Ni_{45}$ alloy was prepared by arc-melting high-purity Ni (99.99%) and enriched 95.73% ^{57}Fe (from Isoflex) under an argon atmosphere. (The intensities of NRIXS and NFS spectra are increased by enriching with the ^{57}Fe isotope, which has a natural abundance of only 2.2%.) Foil samples of 15-20 μm thickness were prepared by cold-rolling the arc-melted ingots, and subsequently annealing at 600°C for 12 hours in vacuum-sealed quartz ampoules. X-ray diffractometry (XRD) was used to confirm the fcc crystal structure of $Fe_{55}Ni_{45}$.

Pieces of approximately 50×50 μm square were cut from the samples and loaded into diamond anvil cells (DACs) for in-situ experiments with NRIXS, NFS, and XRD. The DACs, symmetric-type and panoramic cells, were loaded with pressure transmitting helium using the COMPRES-GSECARS gas loading system (Rivers) as the pressure medium to better ensure hydrostatic pressures at the sample. Beryllium gaskets were used for NRIXS and NFS to minimize the absorption of X-ray and γ-ray signals emitted from the samples. Holes were drilled in the Be gaskets by laser micromachining system to create a sample chamber, using facilities at sector 16 (High-Pressure Collaborative Access Team) of the Advanced Photon Source (APS) [41]. To determine the pressure inside the sample chamber, two ruby spheres were placed near the sample, and a Raman spectrometer was used to measure and analyze their optical fluorescence spectra. The pressure reported is the average of the two ruby spheres.

Synchrotron measurements

The small size of the X-ray beam at the APS allows for measurements on small samples under controlled pressures in DACs. XRD patterns at multiple pressures were measured at beamline 16-BMD (HPCAT) of the APS. The symmetric-type DACs with samples loaded were placed directly in the beam path for measurements at room temperature (RT≃295 K) and in a heating block for measurements at 392 K. Lattice parameters were determined from the (111) diffraction peaks, which gave the strongest intensities and most consistent peak shapes. Peak centers were determined by fitting these peaks to Gaussian functions. $Fe_{55}Ni_{45}$ has a cubic structure, so the unit cell volume was obtained from the lattice parameter cubed. Peak centers were used to quantify how the unit cell volume changed with pressure, and how the material expanded with an increase in temperature of 97 K.

The partial phonon densities of states (DOS) of ^{57}Fe were obtained by NRIXS measurements at beamline 3 ID-B of the APS at Argonne National Laboratory. The NRIXS spectra were collected with three avalanche photodiode detectors positioned at the side openings of the panoramic DACs, perpendicular to the incident X-ray beam. The NRIXS spectra were acquired by scanning the energy of the incident beam across the nuclear resonance of ^{57}Fe at 14.41 keV [42]. The energy resolution of the inelastic spectra was approximately 1.1 meV with the high-resolution monochromator. The PHOENIX software package [43] was used to remove the resonant elastic peak at 14.41 keV, subtract the background, and correct for multiphonon scattering to get the DOS of ^{57}Fe.

The pressure dependence of the ^{57}Fe hyperfine magnetic field (HMF) of $^{57}Fe_{55}Ni_{45}$ was obtained by NFS measurements, also performed at beamline 3 ID-D of the APS. NFS measures the time beats that arise from interferences between γ-ray emissions of different ^{57}Fe nuclei during their transitions from excited to ground states [42]. These time beats are superimposed on an exponential decay from the lifetime of the excited state. The CONUSS software package [43] was used to analyze the beat patterns by fitting with two asymmetrized Gaussians. The mean HMF at each pressure was determined as the average of this model HMF distribution.

4.3 Results

X-Ray lattice parameter, NRIXS, and NFS

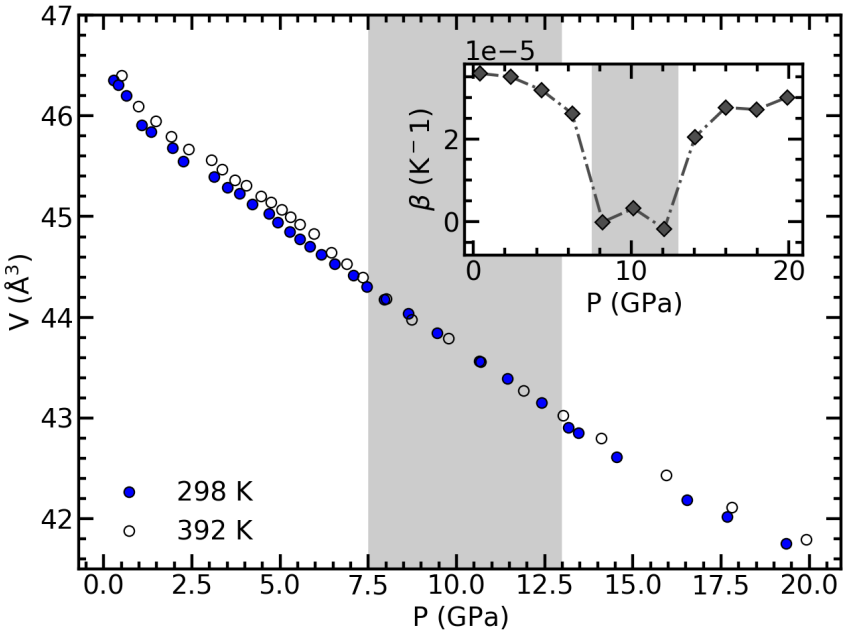

Figure 4.1: Pressure dependence of the unit cell volume of Fe-45%Ni at RT (filled circles) and 392 K (open circles). (Inset) Pressure dependence of the coefficient of thermal expansion (CTE) measured by XRD. A pressure induced Invar effect is observed between 7 GPa and 13 GPa (shaded area).

Figure 4.1 shows the unit cell volume from X-ray lattice parameter data as a function

of pressure and temperature. At pressures below 3 GPa, the curvature of the unit cell volume as a function of pressure, which is inversely related to the bulk modulus, is similar between RT and 392 K. An analysis on the curvature of the unit cell volume as a function of pressure is shown in Fig. 4.10. At pressures between 7 GPa and 13

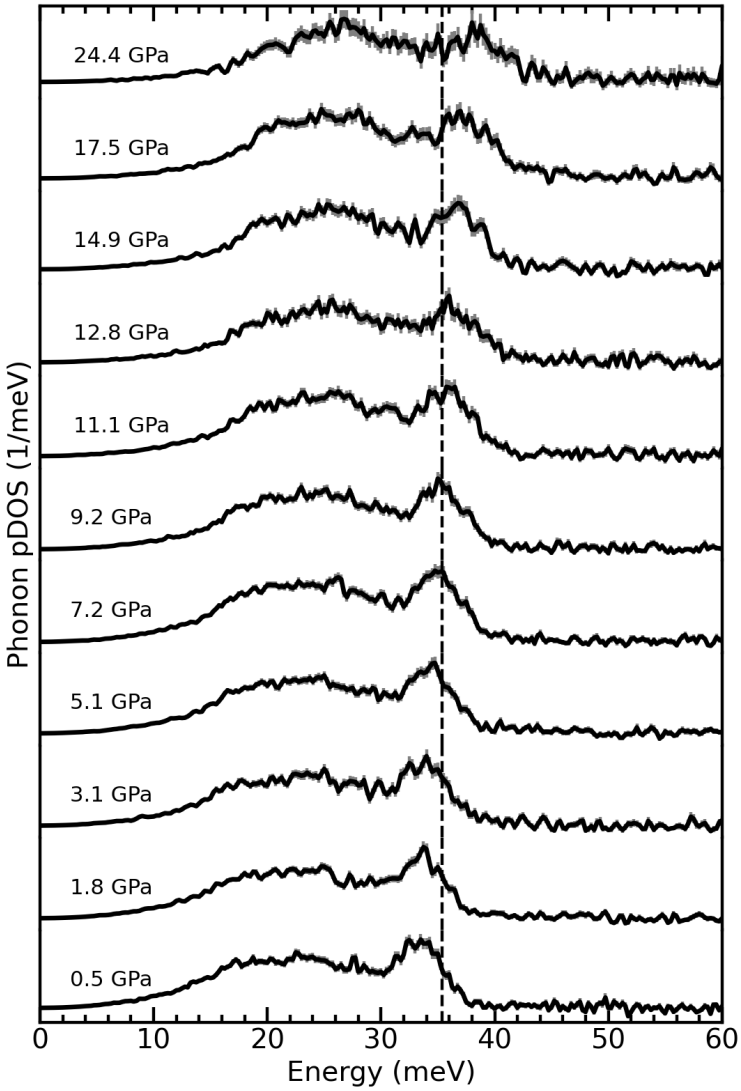

Figure 4.2: Pressure dependence of the ^{57}Fe DOS of Fe-45%Ni obtained by Phoenix software from NRIXS measurements at RT. Vertical dashed line is fixed at the average of the peak position of the longitudinal modes from the 9.2 GPa and 11.1 GPa DOS curves. Error bars are shown in gray.

GPa, the unit cell volume shows no detectable thermal expansion between RT and

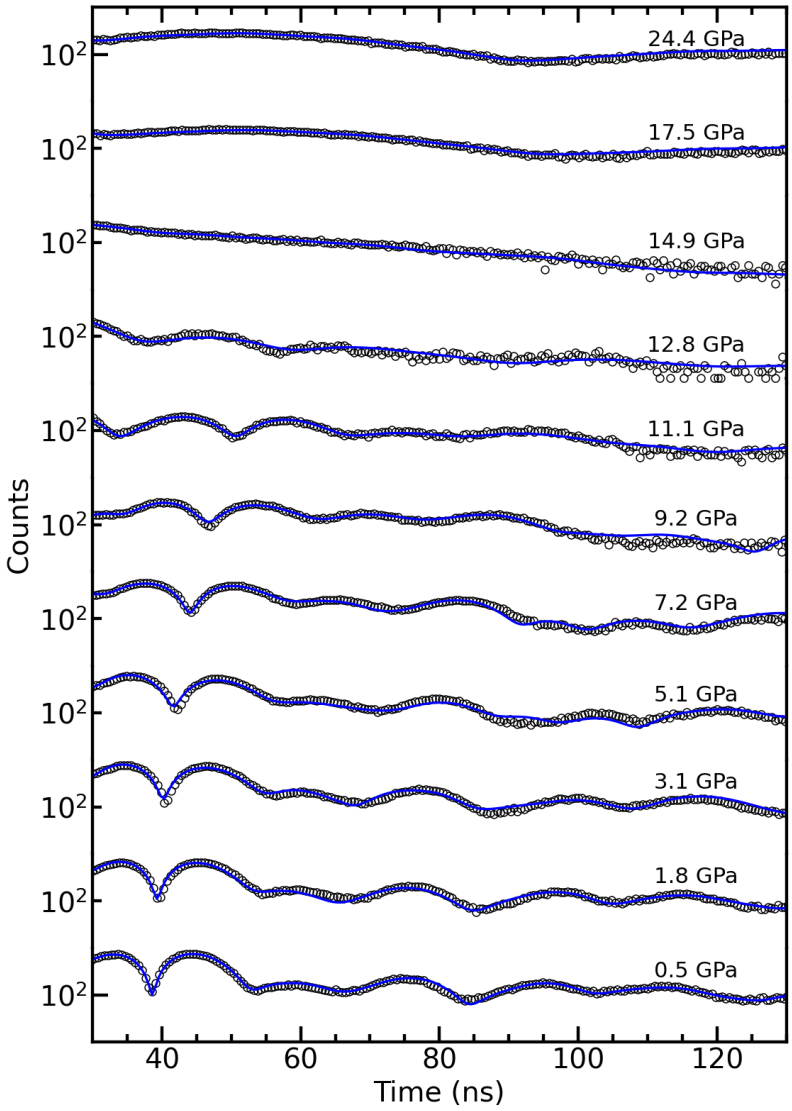

Figure 4.3: Pressure dependence of the time signal of $Fe_{55}Ni_{45}$ measured with NFS at RT, with CONUSS fits (blue solid curves) to the beat patterns.

392 K. At pressures below 7 GPa and above 13 GPa, however, the volume increases with temperature, becoming a more typical $\beta = 3\text{x}10^{-5}K^{-1}$. A spline interpolation was used to determine the difference between the unit cell volume as a function of pressure at RT and 392 K.

The NRIXS and NFS spectra were collected consecutively under the same experimental conditions from the same sample. Figure 4.2 shows phonon DOS curves

measured by NRIXS at pressures up to 24 GPa. These spectra show a general increase in energy with increasing pressure. The vertical dashed line is a reference that shows how there is little change in the center of the peak from longitudinal phonon modes between 7.2 and 12.8 GPa. Pairs of phonon DOS curves, shown in Fig. 4.6, show this same trend.

Figure 4.3 shows the NFS spectra at different pressures. Clear magnetic beat patterns are seen at pressures below 14.9 GPa. The beats spread apart in time as the HMF is reduced by increased pressure. Values of the HMF were obtained from the CONUSS fits shown as the solid lines in Fig. 4.3. This trend is caused by a reduction in HMF with pressure, which is shown in Fig. 4.4.

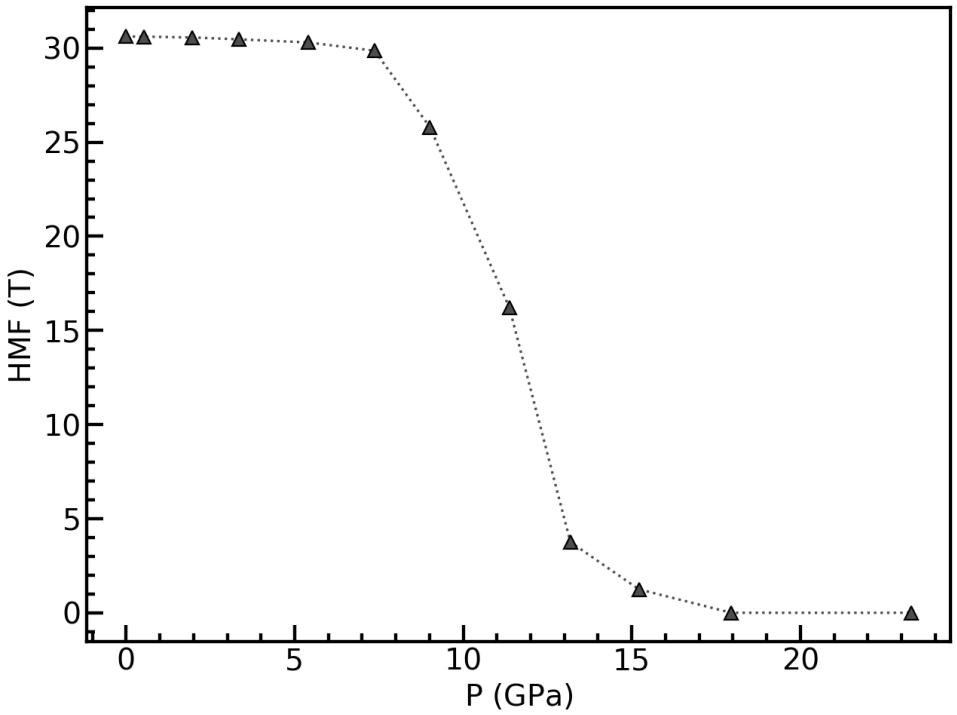

Figure 4.4: Pressure dependence of the HMF in $Fe_{55}Ni_{45}$ quantified from NFS with CONUSS measured at RT.

Phonon Entropy

The NRIXS method is an incoherent scattering that provides the phonon spectrum of the solid projected onto the resonant ^{57}Fe nuclei. Contributions from the other atoms in an alloy are not directly measured in an NRIXS spectrum, and this might be a concern in obtaining a thermodynamic vibrational entropy from an alloy if the other elements differed in their vibrational spectra. Fortunately, a prior study

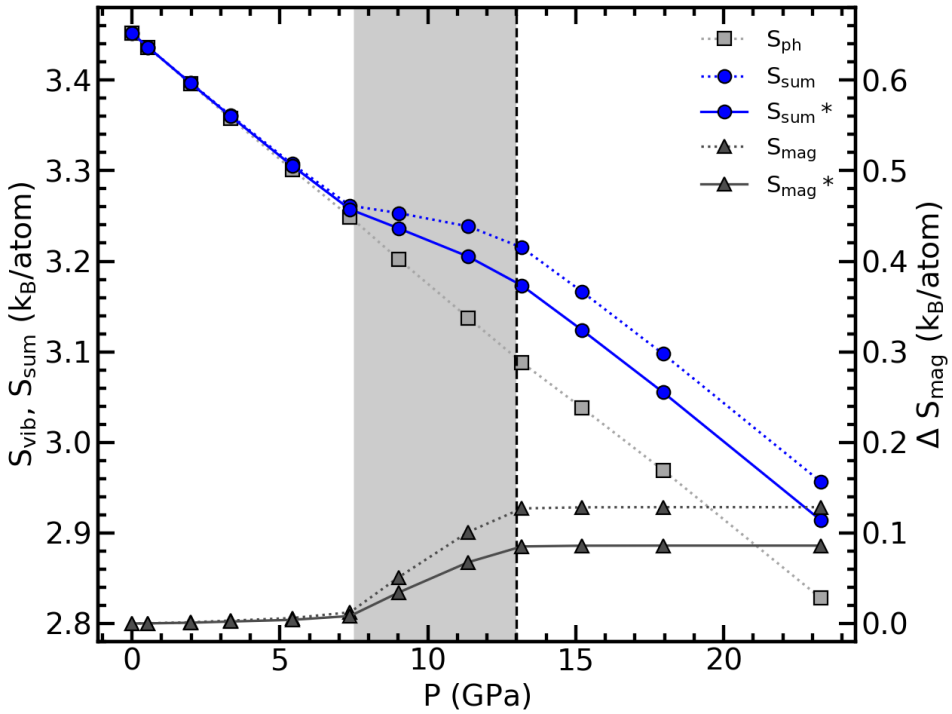

Figure 4.5: Pressure dependence of the vibrational entropy (squares), magnetic entropy (triangles), and their sum (circles) obtained from NRIXS and NFS measured at RT. The shading marks the pressure induced Invar region. Dashed vertical line marks the Curie pressure. S_{mag} and S_{sum} was determined with $S_{mag}^{\Delta T}$ from [44]. The $S_{\mathrm{mag}}{}^{*}$ and $S_{\mathrm{sum}}{}^{*}$ were determined with $S_{mag}^{\Delta T}$ from [5].

compared the inelastic spectra from NRIXS to inelastic neutron scattering spectra of Fe-Ni alloys showed that the phonon partial DOS of Ni and Fe have the same shape [45]. For $Fe_{55}Ni_{45}$, the total phonon DOS is therefore the same as that obtained by

NRIXS. This was also confirmed in recent report [5] by comparing spectra from inelastic neutron scattering and NRIXS for $Fe_{64}Ni_{36}$. The phonon entropy, S_{ph}, is then determined from the phonon DOS, $g(\epsilon)$, as [46]

$$S_{\rm ph} = 3k_{\rm B}\int_0^{\infty} g(\epsilon)\Big[(1+n_{\epsilon,T})\ln(1+n_{\epsilon,T}) - n_{\epsilon,T}\ln n_{\epsilon,T}\Big]\,d\epsilon \tag{4.9}$$

where ϵ is the phonon energy, and $n_{\epsilon,T}$ = 1/(exp($\epsilon/k_{\rm B}T$)-1) is the Planck distribution for phonon occupancy. Figure 4.5 shows the pressure dependence of the $S_{\rm ph}(P)$ obtained from Eq. 4.9 with the phonon DOS data of Fig. 4.2. The curve of $S_{\rm ph}(P)$ vs. P is nearly linear. Subtle deviations from linearity are observed in the range of 7 to 13 GPa, corresponding to the range of the pressure-induced Invar effect.

Effects of Pressure on Phonon DOS Figure 4.6 show phonon DOS curves for $Fe_{55}Ni_{45}$, plotted in pairs of sequential pressure increments. Monotonic behavior of the phonons is observed throughout most of the pressure range. However, between the pressures of 7.2 and 12.8 GPa, the position of the peak from the longitudinal modes remains fixed in energy. The lower part of the phonon DOS, dominate by transverse modes, stiffens consistently with pressure, and does so in the range from 7.2 to 12.8 GPa.

Magnetic Entropy

Figure 4.4 shows the average ^{57}Fe HMF as a function of pressure, obtained from CONUSS fits to the NFS spectra. The HMF is proportional to the magnetic moment of Fe atoms [47], so Fig. 4.4 shows that pressure causes the magnetization to

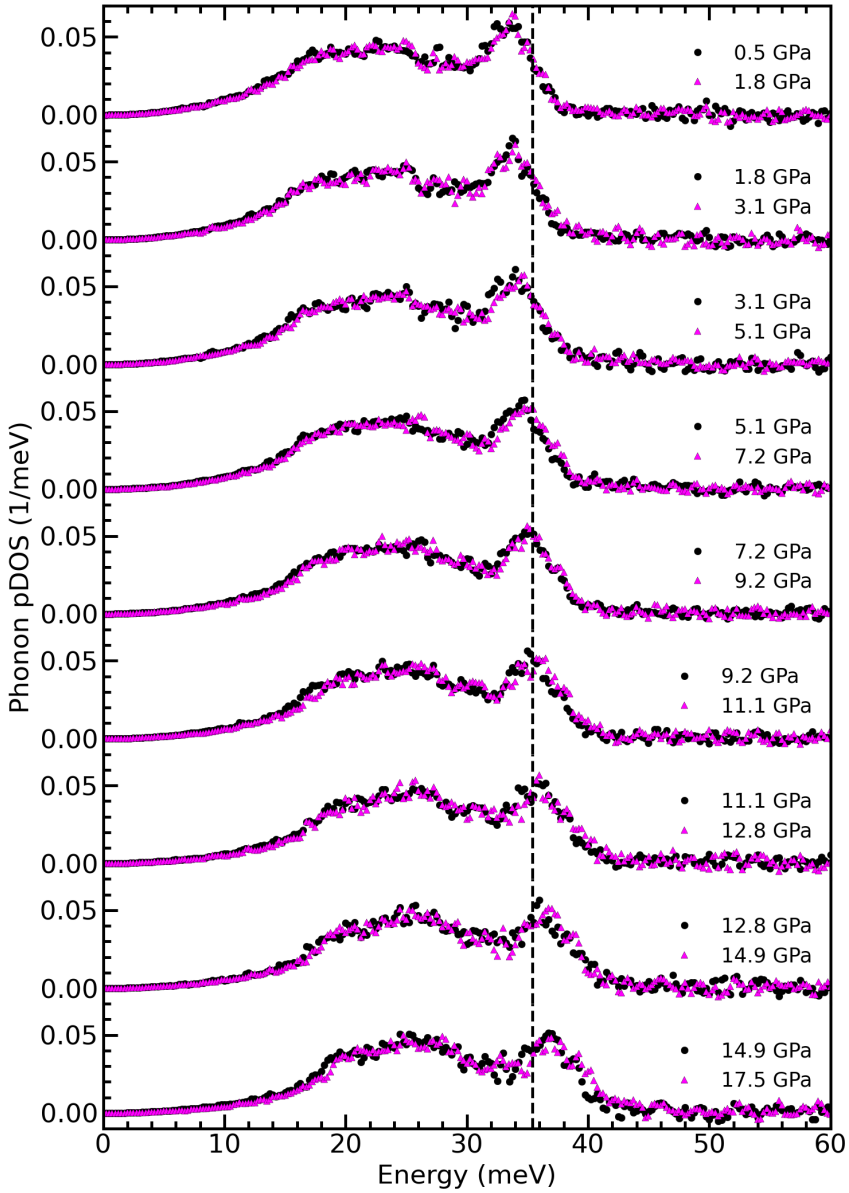

Figure 4.6: ^{57}Fe phonon DOS in $Fe_{55}Ni_{45}$ shown in pairs with pressure differences of approximately 2 GPa. Vertical line is fixed at the average of the peak position of the longitudinal modes from the 9.2 GPa and 11.1 GPa DOS curves.

decrease, and magnetization is lost above the Curie pressure of 13 GPa. The magnetization $M(P)$ and the magnetic entropy S_{mag} were determined from the data of Fig. 4.4 as in [48], which used a mean-field model with spin disordering that

corresponds to the decreasing magnetization $M(P)$

$$\Delta S_{\mathrm{mag}}(P) = -\frac{S_{\mathrm{mag}}^{\Delta \mathrm{T}}}{2\ln 2}\left[(1+\mathrm{M(P)})\ln\left(\frac{1+\mathrm{M(P)}}{2}\right) + (1-\mathrm{M(P)})\ln\left(\frac{1-\mathrm{M(P)}}{2}\right)\right] \tag{4.10}$$

This model does not include magnetic short-range order, and is therefore valid only below the Curie temperature (T_{C}). The change in magnetic entropy from RT to T_{C} ($S_{\mathrm{mag}}^{\Delta \mathrm{T}}$) is obtained from the magnetic heat capacity, and is used to calibrate the change in entropy below the Curie pressure in Eq. 6. It was found in previous experimental studies on fcc Fe-Ni alloys that for concentrations greater than 44.7%-Ni, a significant and inseparable contribution to the specific heat is caused by heat evolution from chemical short-range ordering [44]. It was suggested that it is impractical to extract the magnetic heat capacity from the specific heat for Fe-Ni alloys with Ni concentrations of 44.7% or greater due to chemical short-range ordering. To obtain $S_{\mathrm{mag}}^{\Delta T}$ for $Fe_{55}Ni_{45}$, we averaged the specific heat data for $Fe_{61.1}Ni_{38.9}$ and $Fe_{66.2}Ni_{33.8}$ from [44] because their heat capacities were not influenced by atomic ordering. A $S_{\mathrm{mag}}^{\Delta T} = 0.128\ k_{\mathrm{B}}$/atom was obtained for $S_{\mathrm{mag}}^{\Delta T}$ by averaging the specific heats of 38.9%-Ni and 33.8%-Ni and reducing the average in proportion to the reduced amount of iron in our material. This 0.128 k_{B}/atom is comparable to the value of $S_{mag}^{\Delta T} = 0.086\ k_B$/atom reported in [5], again after scaling their reported value for the iron concentration. The change in entropy below the Curie pressure resulting from the decrease in magnetization as determined from Eq. 6 is shown in Fig. 4.5, for both values of $S_{\mathrm{mag}}^{\Delta T}$.

It is known from [5, 49, 50] that the magnetic structure in Fe rich fcc Fe-Ni alloys is

dominated by the Fe atoms, with only a minor contribution from Ni. From [50, 51] we know that pressure has a minor influence on the alignment of the Ni magnetic moments, and contributes minimally to the magnetic entropy. Therefore, the change in magnetic entropy under pressure $\Delta S_{mag}(P)$ of Fig. 4.5 from NFS accounts for nearly all the change in magnetism in $Fe_{55}Ni_{45}$.

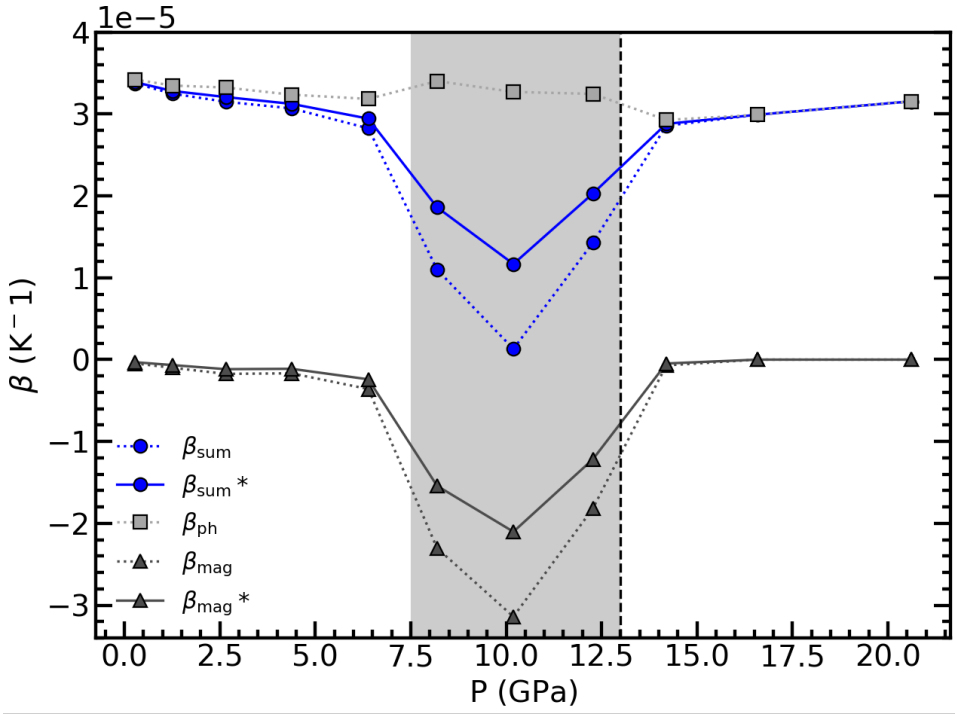

Figure 4.7: Pressure dependence of the coefficient of thermal expansion (CTE) from the individual contributions of phonons (squares), magnetism (triangles), and their sum (circles) to Eq. 4. Shaded area represents the range of pressure induced Invar effect. Dashed vertical line marks the Curie pressure. The β_{mag} and β_{sum} were determined with $S^{\Delta T}_{mag}$ from [44]. The $\beta_{mag}{}^{*}$ and $\beta_{sum}{}^{*}$ was determined with $S^{\Delta T}_{mag}$ from [5].

Temperature Dependence of the Normalized Magnetization The magnetization of an $Fe_{55}Ni_{45}$ sample having a mass of 46 grams is shown in Fig. 4.8. Measurements were performed with a vibrating sample magnetometer in a Physical

Property Measurement System (PPMS by Quantum Design) with an applied magnetic field of 0.1 T from a temperature of 10 K to 400 K. Under ambient conditions, the sample is found to be in a magnetic state equivalent to 90% of the state of full magnetization.When considering a simple Ising model to calculate the entropy associated with magnetic disordering, the 10% of magnetic disorder seen at RT corresponds to 25% of the magnetic entropy that would be measured in a sample that begins in an aligned state and becomes completely demagnetized.

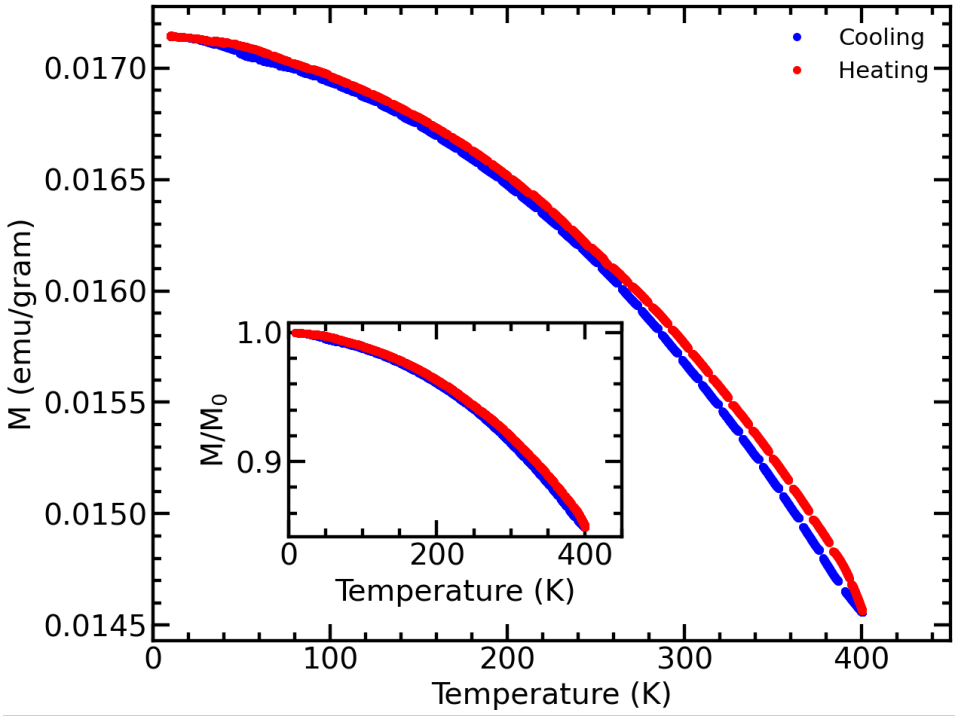

Figure 4.8: $Fe_{55}Ni_{45}$ temperature dependence of the magnetization from 10K to 400 K. The normalized magnetization is shown in the inset.

Hyperfine Magnetic Field Distributions The interference beats observed in nuclear forward scattering (NFS) arise from γ-ray emissions of different ^{57}Fe nuclei transitioning from their excited state back to their ground state. A distribution,

P(HMF), of hyperfine magnetic fields (HMF) can be fit to the beat patterns. The NFS spectra were fitted with two asymmetrized Gaussians and HMF distributions were obtained, shown in Fig. 4.9.

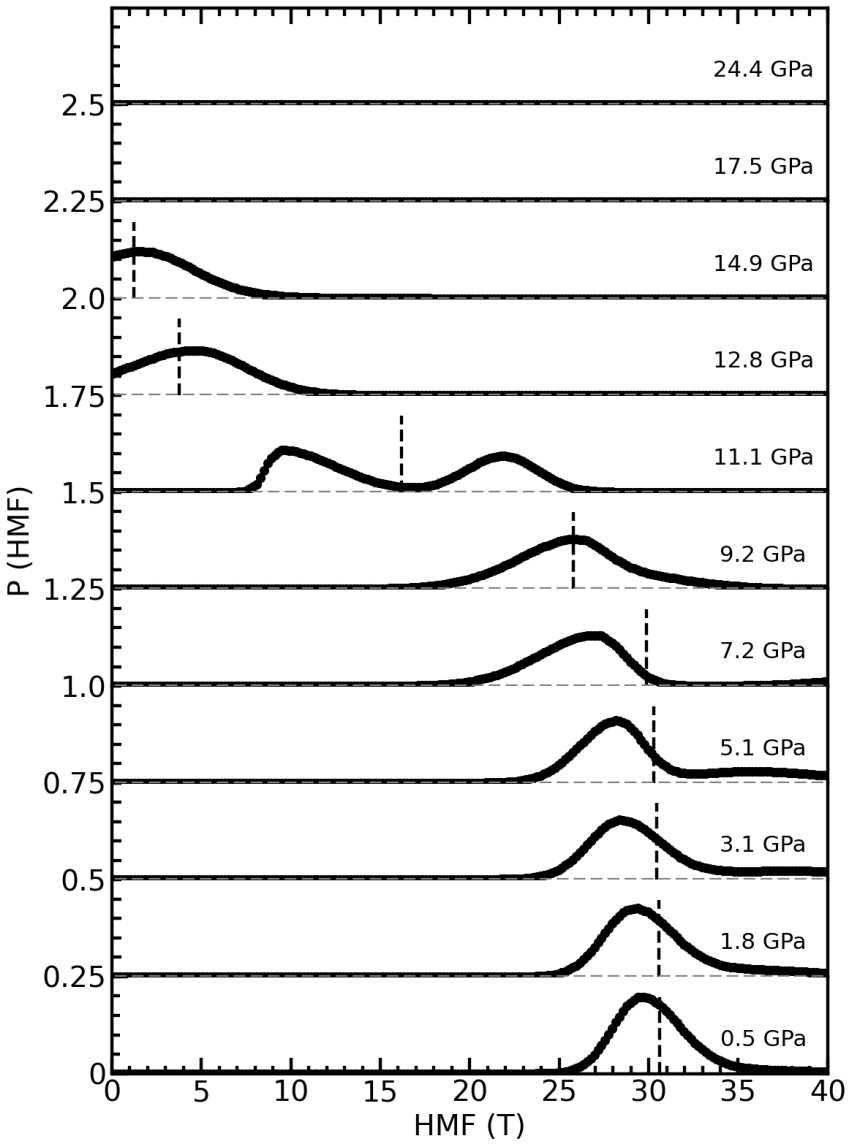

Figure 4.9: $Fe_{55}Ni_{45}$ HMF distribution obtained from CONUSS fits at various pressures. The mean HMF at each pressure is shown by the vertical dashed line.

Temperature Dependence of the Bulk Modulus

Between 0°C and 400°C, nearly constant values of Young's modulus and shear modulus of $Fe_{55.57}Ni_{44.43}$ were reported in previous experimental studies [52]. The bulk modulus can be expressed in terms of Young's modulus and shear modulus using the following equation.

$$B = \frac{EG}{3(3G - E)} \tag{4.11}$$

From the results in [52], the bulk modulus is therefore expected to remain nearly constant with temperature at these temperatures below the Curie transition.

The isothermal bulk modulus is

$$B_T = -V\left(\frac{\partial P}{\partial V}\right)_T \tag{4.12}$$

The bulk modulus was obtained from our pressure-dependent XRD measurements on $Fe_{55}Ni_{45}$ by analyzing the curvature of the unit cell volume as a function of pressure at different temperatures. Results for the pressure dependence of the bulk modulus in $Fe_{55}Ni_{45}$ at room temperature and 392K are shown in Fig. 4.10. The inset of Fig. 4.10 shows the difference in bulk modulus at room temperature and 392K for pressures below 5 GPa. The Elinvar effect is observed for pressures below 3 GPa in $Fe_{55}Ni_{45}$.

Determining a second derivative with the $Fe_{55}Ni_{45}$ entropy data obtained from NFS and NRIXS measurements was attempted and is shown in Fig. 4.11. At pressures below 3 GPa, the temperature dependence of the bulk modulus is near

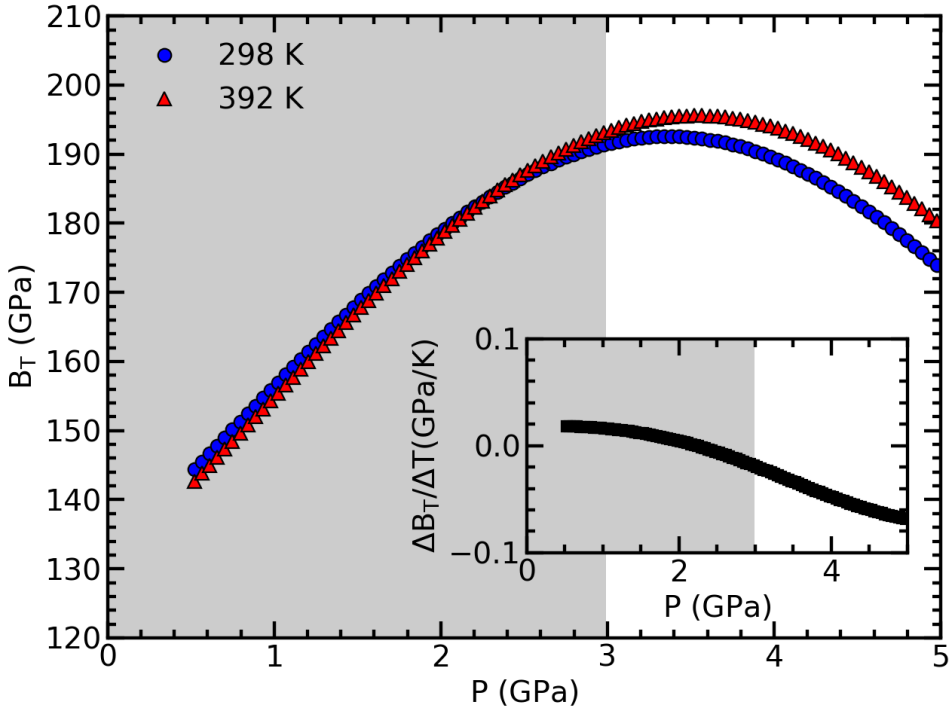

Figure 4.10: Pressure dependence of the isothermal bulk modulus of Fe-45%Ni at RT (blue) and 392 K (red). (Inset) Difference between the bulk modulus at RT and 392.

zero. Interestingly, the magnetic contribution undergoes a large change in sign near 10 GPa.

4.4 Discussion

Figure 4.5 shows the phonon entropy $S_{\mathrm{ph}}(P)$, the change in magnetic entropy $\Delta S_{\mathrm{mag}}(P)$, and their sum, $S_{\mathrm{sum}}(P)$. Between the pressures of 7 and 13 GPa, $S_{\mathrm{sum}}(P)$ is a nearly constant. This pressure range is the region of low thermal expansion observed by synchrotron XRD under pressure (Fig. 4.1 inset). The separate contributions to thermal expansion (β) from phonons, spins, and their sum are shown in Fig. 4.7. Below 7 GPa, $\beta_{\mathrm{ph}}(P)$ is approximately $+3 \times 10^{-5} K^{-1}$ and $\beta_{\mathrm{mag}}(P)$ is negligible. This is again the case for pressures greater than 13 GPa. From

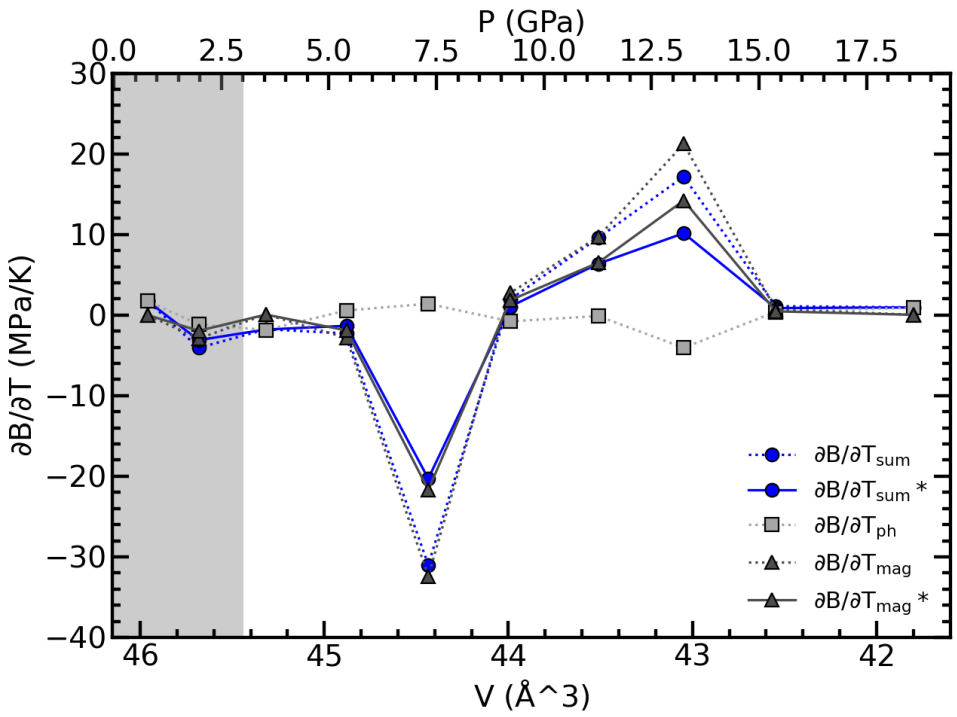

Figure 4.11: Volume and pressure dependence of the isothermal bulk modulus of Fe-45%Ni at RT obtained from NRIXS and NFS measurements. The $\partial B/\partial T_{mag}$ and $\partial B/\partial T_{sum}$ were determined with $S^{\Delta T}_{mag}$ from [44]. The $\partial B/\partial T_{mag}{}^{*}$ and $\partial B/\partial T_{sum}{}^{*}$ was determined with $S^{\Delta T}_{mag}$ from [5].

7 GPa to 13 GPa, the magnitude of $\beta_{ph}(P)$ remains approximately constant, but $\beta_{mag}(P)$ increases to $-3 \times 10^{-5} K^{-1}$. This cancellation of $\beta_{ph}(P)$ from phonons and $\beta_{mag}(P)$ from magnetism accounts for the low thermal expansion in the range of the pressure-induced Invar effect. The magnetic entropy changes most rapidly with pressure just below the Curie pressure, contributing to the thermal expansion by Eq. 4. At pressures above the Curie transition, and well below, phonons are the main source of thermal expansion.

Figure 4.12 shows the coefficient of thermal expansion (CTE) from synchrotron XRD measurements under pressure, compared to the CTE derived from the contributions of phonons and magnetism from Eq. 4. The agreement between the two independent

methods for determining the pressure dependence of thermal expansion is good, with the largest discrepancy being caused by uncertainty in the magnetic entropy of the Curie transition.

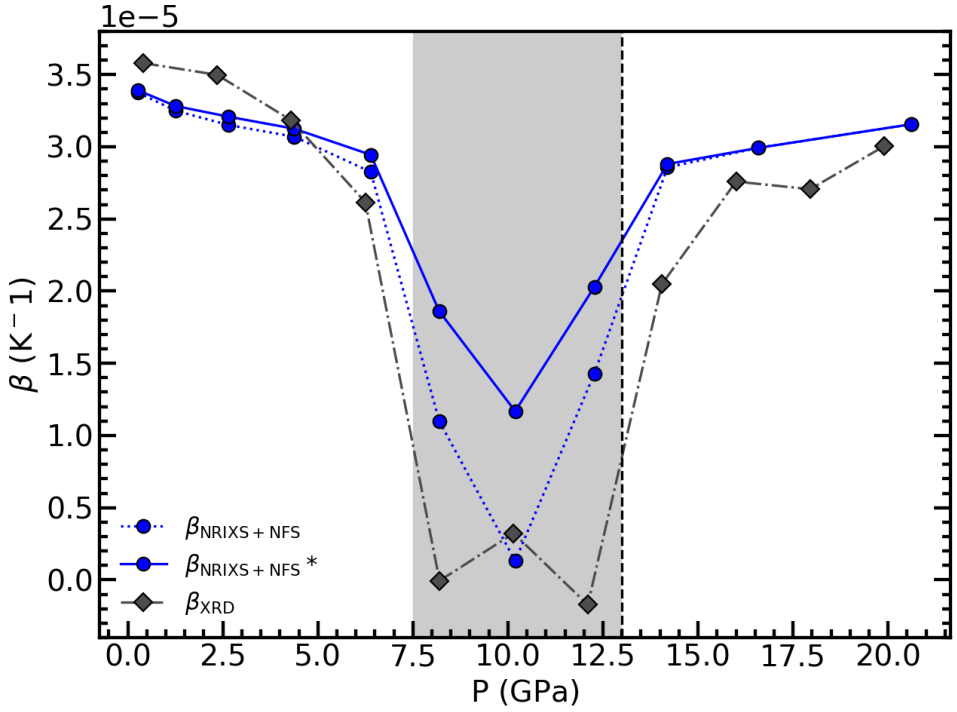

Figure 4.12: Pressure dependence of the coefficient of thermal expansion (CTE) from the individual contributions of phonons and magnetism (circles) compared to the measured CTE by synchrotron XRD (diamonds) Shading marks the region of the pressure-induced Invar effect. $\beta_{\mathrm{NRIXS+NFS}}$ was determined with $S^{\Delta T}_{\mathrm{m}ag}$ values from [44] and $\beta_{\mathrm{NRIXS+NFS}}{}^{*}$ was determined with $S^{\Delta T}_{\mathrm{m}ag}$ values from [5].

The phonon entropy of Fig. 4.5, $S_{\mathrm{p}h}$, is nearly monotonic with pressure. There is an overall stiffening of the phonon DOS at all pressures, and the lower-energy transverse modes seem unaffected by the Curie transition. Changes in the phonon DOS near the Curie pressure, when the magnetization is changing rapidly, are an indication of a spin-phonon interaction. Specifically, in the pressure range of 7.2 to 12.8 GPa, the position of the peak from the longitudinal modes remains nearly

constant and does not increase with pressure. This peak is marked with the vertical dashed line in Fig. 4.2, and Fig. 4.6 shows this by comparing pairs of phonon DOS spectra with differences of 2 GPa in pressure. A similar behavior of the longitudinal peak was found in $Fe_{65}Ni_{35}$ Invar below the Curie pressure, and computational research showed that a spin-phonon interaction was needed to account for it [5]. A definitive proof of a spin-phonon interaction in $Fe_{55}Ni_{45}$ cannot be made solely with the present experimental results, however.

A comparison between the present data on $Fe_{55}Ni_{45}$ and the prior results on $Fe_{65}Ni_{35}$ Invar [5] highlights interesting features of Invar behavior in Fe-Ni. The pressure-induced Invar behavior in $Fe_{55}Ni_{45}$ has a lower bound in pressure, unlike the case for $Fe_{65}Ni_{35}$ Invar, which begins at ambient pressure. Perhaps the key difference between the two materials is that the Curie pressure, P_C, of 13 GPa in $Fe_{55}Ni_{45}$ is higher than the P_C of 4.6 GPa in $Fe_{65}Ni_{35}$ by nearly a factor of three. With total magnetic entropies that are similar, the change of magnetic entropy with pressure is spread over a range in pressure that is approximately three times wider, so the magnetic contribution to thermal expansion should be smaller in $Fe_{55}Ni_{45}$ than in $Fe_{65}Ni_{35}$.

With pressure, the more gradually changing $\partial S_{mag}/\partial P$ for $Fe_{55}Ni_{45}$ is expected to be competitive with the $\partial S_{vib}/\partial P$ at pressures approaching P_C where $M(P)$ changes more rapidly. Indeed, the region of anomalous thermal expansion in $Fe_{55}Ni_{45}$ extends from 7.5 GPa to nearly the P_C of 13 GPa, a range of 5.5 GPa. In contrast, the region of Invar behavior in $Fe_{65}Ni_{35}$ is approximately 0 to 3 GPa, about half

this range. The Invar behavior in $Fe_{65}Ni_{35}$ does not extend to P_C because its $\partial S_{mag}/\partial P$ and $\partial S_{vib}/\partial P$ both become large between 3 and 4.6 GPa. Although they retain their opposite signs, the cancellation of their large magnitudes is not sufficiently precise. The magnetization decreases rapidly in a small pressure range near P_C in $Fe_{65}Ni_{35}$ Invar. Curiously, there is also a significant change in $\partial S_{vib}/\partial P$ from spin-phonon interactions in this same range of magnetic disordering. The evidence for spin-phonon coupling in $Fe_{55}Ni_{45}$ is less distinct because the spins become disordered over a broader range of pressure, and the change in spin-phonon coupling is, therefore, more gradual. It is not clear if the spin-phonon interaction in $Fe_{55}Ni_{45}$ differs significantly from that in $Fe_{65}Ni_{35}$, but its change with pressure is less obvious.

4.5 Conclusion

A pressure-induced Invar effect in $Fe_{55}Ni_{45}$ was confirmed by synchrotron XRD measurements at RT and 392 K, where a low thermal expansion was observed from 7 GPa to 13 GPa. The contributions of phonons and magnetism to the thermal expansion of $Fe_{55}Ni_{45}$ were determined by obtaining entropies of phonons and spins from NRIXS and NFS measurements. From 7 GPa to 13 GPa, a rapid change in magnetic entropy from the disordering of spins was observed, giving a thermal expansion that opposed the more monotonic contribution of thermal expansion from phonons. The pressure-induced Invar effect in $Fe_{55}Ni_{45}$ is a consequence of this cancellation of the thermodynamic contributions to thermal expansion from phonons and spins. The phonon DOS of $Fe_{55}Ni_{45}$ showed an arrest of the stiffening with

pressure of the longitudinal phonon modes, indicative of a spin-phonon coupling.

References

[1] C.-É. Guillaume, *Recherches sur les aciers au nickel*. Gauthier-Villars, 1897.

[2] C.-É. Guillaume, "The anomaly of the nickel-steels," *Proceedings of the Physical Society of London*, vol. 32, no. 1, p. 374, 1919.

[3] C.-É. Guillaume, "Nobel Lecture in Physics," https://www.nobelprize.org/uploads/2018/06/guillaume-lecture.pdf, 1920.

[4] E. Wasserman, "Invar: Moment-volume instabilities in transition metals and alloys," *Handbook of Ferromagnetic Materials*, vol. 5, pp. 237–322, 1990.

[5] S. H. Lohaus, M. Heine, P. Guzman, C. M. Bernal-Choban, C. N. Saunders, G. Shen, O. Hellman, D. Broido, and B. Fultz, "A thermodynamic explanation of the invar effect," *Nature Physics*, vol. 19, no. 11, pp. 1642–1648, 2023.

[6] K. Sumiyama, M. Shiga, M. Morioka, and Y. Nakamura, "Characteristic magnetovolume effects in Invar type Fe-Pt alloys," *Journal of Physics F: Metal Physics*, vol. 9, no. 8, p. 1665, 1979.

[7] Y. Nakamura, K. Sumiyama, and M. Shiga, "Fe-Pt Invar alloys—homogeneous strong ferromagnets," *Journal of Magnetism and Magnetic Materials*, vol. 12, no. 2, pp. 127–134, 1979.

[8] M. Takahashi, F. Ono, and K. Takakura, "The Invar characteristics on Co-Fe alloys," *AIP Conference Proceedings*, vol. 29, no. 1, pp. 562–563, 1976.

[9] B. Gehrmann, M. Acet, H. Herper, E. Wassermann, and W. Pepperhoff, "The Invar property of elemental fcc Co and large spontaneous magnetostriction of bcc Fe-Co," *physica status solidi (b)*, vol. 214, no. 1, pp. 175–185, 1999.

[10] G. Hausch, "Invar-like thermal expansion anomaly in antiferromagnetic Mn-Ni alloys," *physica status solidi (a)*, vol. 41, no. 1, pp. K35–K38, 1977.

[11] T. Yokoyama and K. Eguchi, "Anisotropic thermal expansion and cooperative Invar and anti-Invar effects in Mn alloys," *Physical Review Letters*, vol. 110, no. 7, p. 075901, 2013.

[12] Y. V. Ergin, "Anomalies in the temperature dependence of the thermal expansion coefficient of a gadolinium single crystal," *Soviet Physics JETP*, vol. 21, no. 4, pp. 709–710, 1965.

[13] R. M. Bozorth and T. Wakiyama, "Magnetostriction and anomalous thermal expansion of single crystals of gadolinium," *Journal of the Physical Society of Japan*, vol. 18, no. 1, pp. 97–106, 1963.

[14] F. Barson, S. Legvold, and F. H. Spedding, "Thermal expansion of rare earth metals," *Physical Review*, vol. 105, no. 2, p. 418, 1957.

[15] A. V. Ruban, S. Khmelevskyi, P. Mohn, and B. Johansson, "Magnetic state, magnetovolume effects, and atomic order in $Fe_{65}Ni_{35}$ Invar alloy: A first principles study," *Physical Review B*, vol. 76, no. 1, p. 014420, 2007.

[16] A. Menshikov, "On the Invar problem," *Physica B: Condensed Matter*, vol. 161, no. 1-3, pp. 1–8, 1990.

[17] A. Sahoo and V. Medicherla, "Fe-Ni Invar alloys: A review," *Materials today: proceedings*, vol. 43, pp. 2242–2244, 2021.

[18] E. Wassermann, "The Invar problem," *Journal of magnetism and magnetic materials*, vol. 100, no. 1-3, pp. 346–362, 1991.

[19] Y. Nakamura, "The Invar problem," *IEEE Transactions on Magnetics*, vol. 12, no. 4, pp. 278–291, 1976.

[20] L. Dubrovinsky, N. Dubrovinskaia, I. A. Abrikosov, M. Vennström, F. Westman, S. Carlson, M. van Schilfgaarde, and B. Johansson, "Pressure-induced invar effect in Fe-Ni alloys," *Physical Review Letters*, vol. 86, no. 21, p. 4851, 2001.

[21] M. Winterrose, M. Lucas, A. Yue, I. Halevy, L. Mauger, J. Muñoz, J. Hu, M. Lerche, and B. Fultz, "Pressure-induced invar behavior in Pd_3Fe," *Physical Review Letters*, vol. 102, no. 23, p. 237202, 2009.

[22] M. Winterrose, L. Mauger, I. Halevy, A. Yue, M. Lucas, J. Munoz, H. Tan, Y. Xiao, P. Chow, W. Sturhahn *et al.*, "Dynamics of iron atoms across the pressure-induced invar transition in Pd_3Fe," *Physical Review B*, vol. 83, no. 13, p. 134304, 2011.

[23] J. Leger, C. Loriers-Susse, and B. Vodar, "Pressure effect on the curie temperatures of transition metals and alloys," *Physical Review B*, vol. 6, no. 11, p. 4250, 1972.

[24] G. Hausch, "Magnetovolume effects in invar alloys: Pressure dependence of the curie temperature," *physica status solidi (a)*, vol. 16, no. 2, pp. 371–376, 1973.

[25] G. Oomi and N. Mori, "High pressure x-ray study of anomalous bulk modulus of an $Fe_{70}Ni_{30}$ invar alloy," *Journal of the Physical Society of Japan*, vol. 50, no. 4, pp. 1043–1044, 1981.

[26] M. Abd-Elmeguid, B. Schleede, and H. Micklitz, "Pressure-induced antiferromagnetism in fcc Fe-Ni invar alloys," *Journal of magnetism and magnetic materials*, vol. 72, no. 3, pp. 253–257, 1988.

[27] M. Abd-Elmeguid and H. Micklitz, "Observation of a pressure-induced collapse of the Fe magnetic moment in the strong itinerant ferromagnet $Fe_{72}Pt_{28}$," *Physical Review B*, vol. 40, no. 10, p. 7395, 1989.

[28] Y. Abdu, H. Annersten, L. Dubrovinsky, and N. Dubrovinskaia, "High pressure mössbauer studies on fcc $Fe_{53}Ni_{47}$ alloy," *Hyperfine Interactions*, vol. 156, pp. 389–394, 2004.

[29] L. Mañosa, G. Saunders, H. Rahdi, U. Kawald, J. Pelzl, and H. Bach, "Acoustic-mode vibrational anharmonicity related to the anomalous thermal expansion of invar iron alloys," *Physical Review B*, vol. 45, no. 5, p. 2224, 1992.

[30] M. Schwoerer-Böhning, S. Klotz, J. Besson, E. Burkel, M. Braden, and L. Pintschovius, "The pressure dependence of the TA1 [110] phonon frequencies in the ordered invar alloy fe3pt at pressures up to 7 GPa," *Europhysics Letters*, vol. 33, no. 9, p. 679, 1996.

[31] S. Odin, F. Baudelet, J. Itié, A. Polian, S. Pizzini, A. Fontaine, C. Giorgetti, E. Dartyge, and J. Kappler, "Experimental evidence of pressure-induced magnetic phase transition in $Fe_{72}Pt_{28}$ invar alloy," *Journal of applied physics*, vol. 83, no. 11, pp. 7291–7293, 1998.

[32] S. Odin, F. Baudelet, C. Giorgetti, E. Dartyge, J. Itié, A. Polian, J. Chervin, S. Pizzini, A. Fontaine, and J. Kappler, "Magnetic phase transitions in $Fe_{72}Pt_{28}$ invar compound studied by high-pressure X-ray magnetic circular dichroism and X-ray diffraction," *Europhysics Letters*, vol. 47, no. 3, p. 378, 1999.

[33] J.-P. Rueff, A. Shukla, A. Kaprolat, M. Krisch, M. Lorenzen, F. Sette, and R. Verbeni, "Magnetism of invar alloys under pressure examined by inelastic X-ray scattering," *Physical Review B*, vol. 63, no. 13, p. 132409, 2001.

[34] M. Matsushita, T. Nishimura, S. Endo, M. Ishizuka, K. Kindo, and F. Ono, "Anomalous magnetic moments in Fe–Pt and Fe–Pd invar alloys under high pressure," *Journal of Physics: Condensed Matter*, vol. 14, no. 44, p. 10753, 2002.

[35] M. Matsushita, S. Endo, K. Miura, and F. Ono, "Pressure-induced change of the magnetic state in ordered Fe–Pt invar alloy," *Journal of Magnetism and Magnetic Materials*, vol. 269, no. 3, pp. 393–397, 2004.

[36] M. Matsushita, Y. Nakamoto, E. Suzuki, Y. Miyoshi, H. Inoue, S. Endo, T. Kikegawa, and F. Ono, "The lattice softening and the crystal structure of Fe–Pt invar alloys under high pressures," *Journal of Magnetism and Magnetic Materials*, vol. 284, pp. 403–408, 2004.

[37] M. Matsushita, Y. Miyoshi, S. Endo, and F. Ono, "Pressure-induced magnetic phase transitions in Fe-based invar alloys," *Physical Review B*, vol. 72, no. 21, p. 214404, 2005.

[38] F. Decremps and L. Nataf, "Abrupt discontinuity of the bulk modulus pressure dependence in $Fe_{64}Ni_{36}$," *Physical Review Letters*, vol. 92, no. 15, p. 157204, 2004.

[39] L. Nataf, F. Decremps, M. Gauthier, and B. Canny, "High-pressure structural study of $Fe_{64}Ni_{36}$ and $Fe_{72}Pt_{28}$ invar alloys at low-temperature," *Physical Review B*, vol. 74, no. 18, p. 184422, 2006.

[40] P. Gorria, D. Martínez-Blanco, M. J. Pérez, J. A. Blanco, A. Hernando, M. A. Laguna-Marco, D. Haskel, N. Souza-Neto, R. I. Smith, W. G. Marshall *et al.*, "Stress-induced large curie temperature enhancement in $Fe_{64}Ni_{36}$ invar alloy," *Physical Review B*, vol. 80, no. 6, p. 064421, 2009.

[41] R. Hrubiak, S. Sinogeikin, E. Rod, and G. Shen, "The laser micro-machining system for diamond anvil cell experiments and general precision machining applications at the high pressure collaborative access team," *Review of Scientific Instruments*, vol. 86, no. 7, 2015.

[42] W. Sturhahn, "Nuclear resonant spectroscopy," *Journal of Physics: Condensed Matter*, vol. 16, no. 5, p. S497, 2004.

[43] W. Sturhahn, "Conuss and phoenix: Evaluation of nuclear resonant scattering data," *Hyperfine Interactions*, vol. 125, no. 1-4, pp. 149–172, 2000.

[44] Y. Tanji, H. Asano, and H. Moriya, "Specific heats of Fe-Ni(fcc) alloys at high temperatures," *Science Rep. Research Inst. Tohoku Univ.*, vol. 24, no. 5, pp. 205–217, 1973.

[45] M. Lucas, L. Mauger, J. A. Munoz, I. Halevy, J. Horwath, S. Semiatin, S. Leontsev, M. B. Stone, D. L. Abernathy, Y. Xiao *et al.*, "Phonon densities of states of face-centered-cubic Ni-Fe alloys," *Journal of Applied Physics*, vol. 113, no. 17, 2013.

[46] B. Fultz, *Phase transitions in materials*. Cambridge University Press, 2020.

[47] M. Kobeissi, "Mössbauer study of static and dynamic critical behavior in Fe," *Physical Review B*, vol. 24, no. 5, p. 2380, 1981.

[48] S. H. Lohaus, M. B. Johnson, P. F. Ahnn, C. N. Saunders, H. L. Smith, M. A. White, and B. Fultz, "Thermodynamic stability and contributions to the gibbs free energy of nanocrystalline Ni_3Fe," *Physical Review Materials*, vol. 4, no. 8, p. 086002, 2020.

[49] I. A. Abrikosov, A. E. Kissavos, F. Liot, B. Alling, S. Simak, O. Peil, and A. V. Ruban, "Competition between magnetic structures in the Fe rich fcc FeNi alloys," *Physical Review B*, vol. 76, no. 1, p. 014434, 2007.

[50] M. van Schilfgaarde, I. Abrikosov, and B. Johansson, "Origin of the invar effect in iron–nickel alloys," *Nature*, vol. 400, no. 6739, pp. 46–49, 1999.

[51] K. Matsumoto, H. Maruyama, N. Ishimatsu, N. Kawamura, M. Mizumaki, T. Irifune, and H. Sumiya, "Noncollinear spin structure in Fe–Ni invar alloy probed by magnetic exafs at high pressure," *Journal of the Physical Society of Japan*, vol. 80, no. 2, p. 023709, 2011.

[52] Y. Tanji, Y. Shirakawa, and H. Moriya, "Youngs modulus, shear modulus, and compressibility of Fe-Ni fcc alloys," *J Japan Inst Metals*, vol. 34, no. 4, pp. 417–421, 1970.

Chapter 5

CONCLUDING REMARKS AND OUTLOOK

This thesis begins with the development of a miniaturized piezoelectric Mössbauer spectrometer controlled by feedback. The optimization of the piezoelectric Doppler drive is achieved through measurements from a laser Doppler vibrometer (LDV). Minimal distortions are observed in the Mössbauer spectra of α-iron in transmission geometry, demonstrating that the performance of the feedback-controlled piezoelectric Doppler drive closely resembles that of a conventional electromagnetic Doppler velocity drive. The outcome of this study enables the application of Mössbauer spectrometry in scenarios requiring small size, mass, and cost. With iron being the most abundant element in the solar system, the creation of a compact and lightweight Mössbauer spectrometer is fundamental for exploring lunar and Martian surfaces. The reduction in mass by a factor of 20 between the piezoelectric actuator's mass (0.19 kg) used in this work and the conventional Mössbauer velocity transducer's mass (4.5 kg) could potentially make the construction of an ultraminiature lightweight Mössbauer spectrometer possible. However, further research and development may be necessary to confirm this possibility.

This thesis also presents the investigation of the interaction between spins and phonons at high pressures in the fcc alloy $Fe_{55}Ni_{45}$. The entropic contribution to the thermal expansion of spins and phonons is determined using nuclear forward scattering (NFS) and nuclear resonant inelastic X-ray scattering (NRIXS) measure-

ments. A rapid decrease in the ^{57}Fe magnetic moment is observed between 7 GPa and 13 GPa with NFS measurements, resulting in a sudden change in magnetic entropy. NRIXS measurements provide the ^{57}Fe phonon density of states (DOS), showing a more steady change in phonon entropy. The thermal expansion contributions from spins and phonons were determined using Maxwell relations. The results suggest that the pressure-induced Invar effect in $Fe_{55}Ni_{45}$ is attributed to the rapid disordering of spins that oppose the monotonic change in phonons.

Additionally, the alloy $Fe_{55}Ni_{45}$ is known as "Elinvar" because it exhibits no change in elastic constants with temperature near ambient conditions. The temperature dependence of the bulk modulus at various pressures is determined directly from X-ray diffraction (XRD) measurements, confirming the Elinvar behavior at low pressures. It was demonstrated that the bulk modulus's temperature dependence is proportional to a second derivative of entropy with volume. From NFS and NRIXS measurements, a second derivative of entropy with volume was determined, which indicated that Elinvar behavior happens at low pressures. However, the results from NFS and NRIXS measurements were not precise enough to determine its thermodynamic origins.

5.1 Outlook

Mössbauer spectrometry is not exclusive to the ^{57}Fe isotope; it can be utilized with other Mössbauer active isotopes such as ^{119}Sn, ^{151}Eu, ^{121}Sb, and ^{161}Dy. Nuclear resonant scattering methods are powerful tools that can be used to investigate the pressure and temperature dependencies of thermophysical properties through

phonons and spins. These techniques include nuclear resonant inelastic X-ray scattering (NRIXS) and nuclear forward scattering (NFS), which can be combined with diamond-anvil cells (DACs) and various temperature control methods. The potential extension of our experimental research direction is now discussed.

Anti-Invar Effect in Fe-Ni and Fe-Mn Alloys

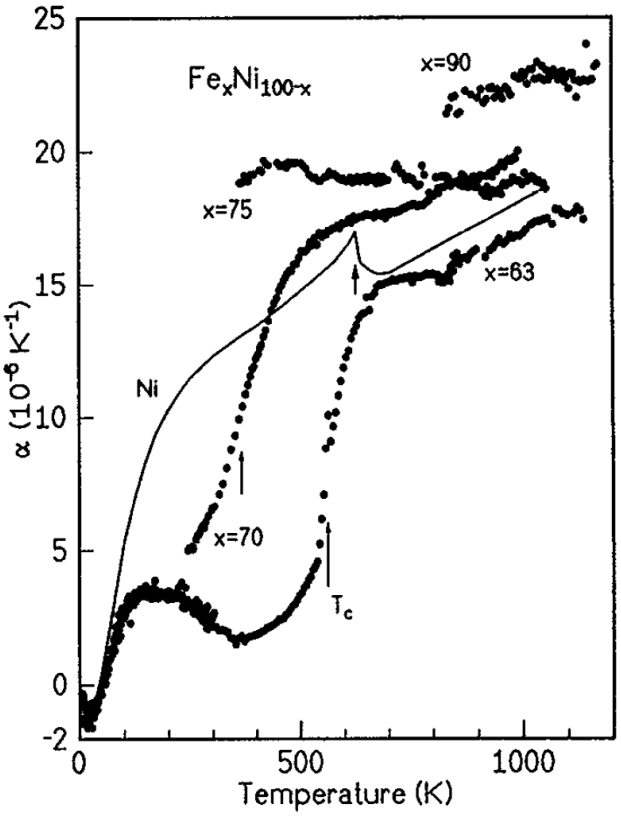

Figure 5.1: Thermal expansion coefficient $\alpha(T)$ for various Fe-Ni alloys. The Curie temperature is identified by the arrows. [1]

An appropriate direction could be the experimental analysis of the anti-Invar Fe-Ni and Fe-Mn systems [1, 2]. The anti-Invar effect is an abnormally high thermal expansion coefficient observed over a wide range of temperatures. This feature is also present in γ-Fe, γ-Mn, and YMn_2 [3, 4]. However, for γ-Fe its stability is

limited between 1200 K to 1700 K [5], making high-pressure NRIXS and NFS measurements challenging. An ideal material for these studies should preserve structural phase stability over the temperature or pressure range of interest and show a magnetic transition from ferromagnetic (FM) or antiferromagnetic (AFM) to paramagnetic (PM). $Fe_{70}Ni_{30}$ fulfills these criteria and displays intriguing thermal expansion behavior. Below the Curie transition, it has low thermal expansion, while above the Curie transition, the expansion becomes considerably large, resembling the anti-Invar effect [1] (see Fig. 5.1). $Fe_{70}Mn_{30}$ also qualifies as a suitable candidate

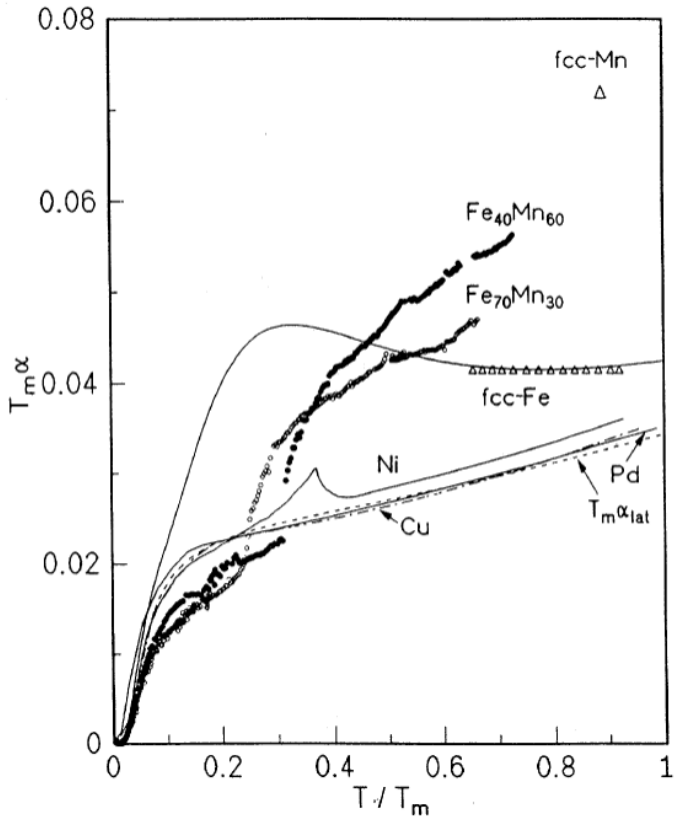

Figure 5.2: The product of the thermal expansion coefficient α and the melting temperature T_m as a function of reduced temperature (T/T_m) for Fe, Ni, Cu, Pd, Mn, $Fe_{60}Mn_{40}$, and $Fe_{70}Mn_{30}$. [2]

material with thermal expansion behavior similar to $Fe_{70}Ni_{30}$, shifting from low to

large thermal expansion at the Néel transition [2] (see Fig. 5.2).

The interaction between phonons and spins through their magnetic transitions in these materials could potentially provide a thermodynamic explanation for the anti-Invar effect. The magnetic entropy should be at its maximum above the Curie or Néel transition, which implies a possible larger role for phonons in the anti-Invar effect. This is in contrast to the pressure-induced Invar effect, where thermal expansion is predominantly suppressed by spins, as discussed in Chapter 4.

Thermal Expansion Anomalies in Rare-Earth Metals

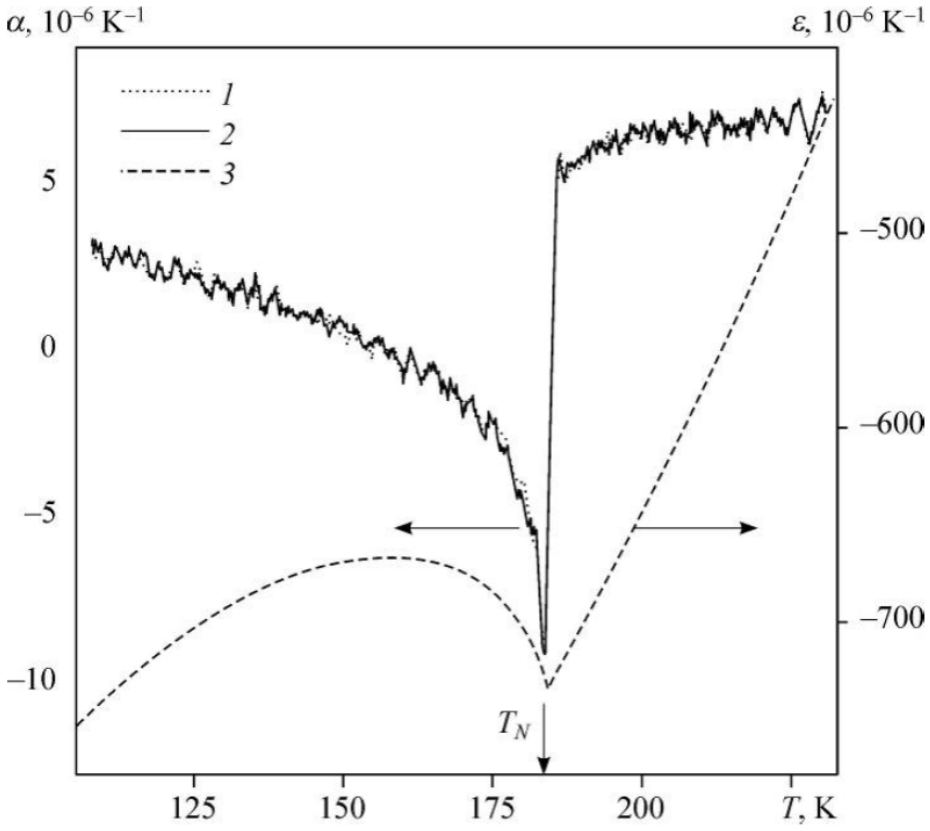

Figure 5.3: Thermal expansion coefficient $\alpha(T)$ for dysprosium. Dashed line represents the relative expansion (ϵ). The Néel temperature is identified by the arrow. [6]

Rare-earth metals such as Gd, Tb, and Dy exhibit anomalous thermal expansion behavior [7]. Some rare-earth metal isotopes, including ^{151}Eu and ^{161}Dy, have been utilized in synchrotron experiments as they are Mössbauer active. The large magnetic moments in Eu, Gd, Tb, Dy, Ho, and Er make these metals interesting for studying phonon and spin behavior through their magnetic transitions [8]. A previously conducted study by [6] reported large negative thermal expansion in dysprosium, as shown in Figure 5.3. Dysprosium, with an antiferromagnetic (AFM) nature, is ideal for ^{161}Dy synchrotron work since its Néel temperature of 180 K is in a feasible temperature range. Examining the magnetic entropy near the Néel transition with increasing temperature or pressure would be interesting, as it is expected to have a direct effect on thermal expansion.

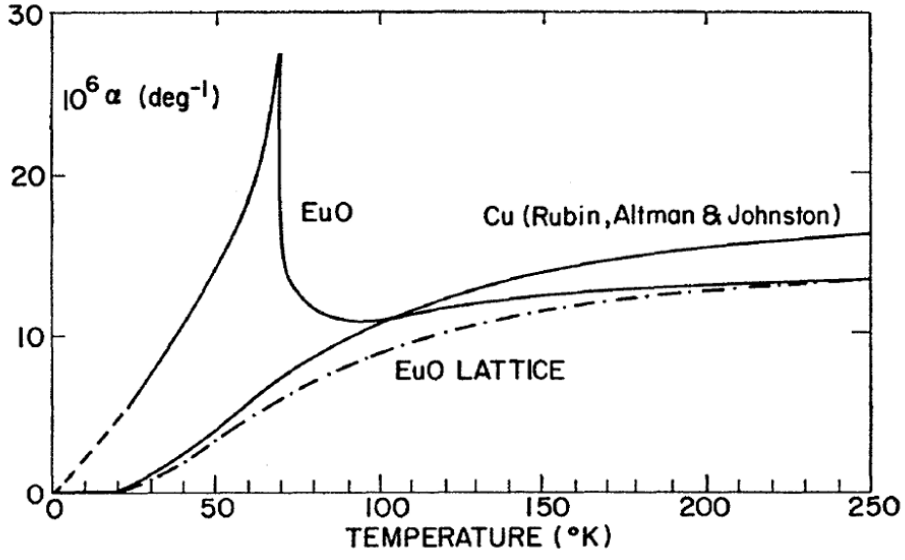

Figure 5.4: Thermal expansion coefficient $\alpha(T)$ for EuO and Cu. Dot-dashed line represents an approximate lattice contribution for EuO. [9]

EuO, a ferromagnetic (FM) semiconductor, is an intriguing material for ^{151}Eu syn-

chrotron experiments due to its anomalous thermal expansion. Its thermal expansion displays an exceptional increase near its Curie temperature [9], as opposed to the typical suppression seen in iron-based Invar alloys. This makes EuO a great candidate for exploring the relationship between spins and phonons.

References

[1] M. Acet, T. Schneider, H. Zähres, E. Wassermann, and W. Pepperhoff, "Anti-Invar in Fe-Ni," *Journal of Applied Physics*, vol. 75, no. 10, pp. 7015–7017, 1994.

[2] T. Schneider, M. Acet, B. Rellinghaus, E. Wassermann, and W. Pepperhoff, "Antiferromagnetic Invar and anti-Invar in Fe-Mn alloys," *Physical Review B*, vol. 51, no. 14, p. 8917, 1995.

[3] M. Acet, H. Zähres, W. Stamm, E. Wassermann, and W. Pepperhoff, "The study of the thermal properties of γ-Mn from Mn-Cu alloys," *Physica B: Condensed Matter*, vol. 161, no. 1-3, pp. 67–71, 1990.

[4] M. Shiga, "Invar alloys," *Current Opinion in Solid State and Materials Science*, vol. 1, no. 3, pp. 340–348, 1996.

[5] R. Boehler, "The phase diagram of iron to 430 kbar," *Geophysical Research Letters*, vol. 13, no. 11, pp. 1153–1156, 1986.

[6] Y. M. Kozlovskii and S. Stankus, "The density and thermal expansion of dysprosium in the temperature range 110–1950 K," *Thermophysics and Aeromechanics*, vol. 22, no. 4, pp. 501–508, 2015.

[7] F. Barson, S. Legvold, and F. H. Spedding, "Thermal expansion of rare earth metals," *Physical Review*, vol. 105, no. 2, p. 418, 1957.

[8] W. C. Koehler, "Magnetic properties of rare-earth metals and alloys," *Journal of Applied Physics*, vol. 36, no. 3, pp. 1078–1087, 1965.

[9] B. Argyle, N. Miyata, and T. Schultz, "Magnetoelastic behavior of single-crystal europium oxide. I. thermal expansion anomaly," *Physical Review*, vol. 160, no. 2, p. 413, 1967.